Chapter 2
Dielectric Nanomaterials for Silicon Solar Cells

Ingo Dirnstorfer and Thomas Mikolajick

Abstract Dielectric nanomaterials are emerging as key components in today's highly efficient silicon solar cells. The most successful materials are SiO_2, SiN_x:H and Al_2O_3 due to their excellent material properties for surface passivation and light management. Dielectric passivation layers ensure high level of chemical passivation by effectively reducing the density of silicon surface states, which could act as recombination centers for photo-generated charge carriers. Additionally, these materials provide strong field-effect passivation by a high density of intrinsic fixed charges. However, novel solar cell concepts demand for dielectric nanomaterials with additional functionalities, such as electrical conductivity, simultaneous applicability on *n*- and *p*-type substrates or compatibility with low-thermal budget processing. Recent developments show that these functionalities can be realized in multi-oxide nanolaminates including HfO_2 or TiO_2 sublayers. Additionally, alternative deposition techniques and innovative processes, such as flash light annealing, become available to reduce process complexity and thermal budget. This chapter reviews the theory and application of dielectric nanomaterials in today's solar cells and gives an outlook on promising solutions in future solar cells.

I. Dirnstorfer (✉) · T. Mikolajick
NaMLab gGmbH, Nöthnitzer Strasse 64, 01187 Dresden, Germany
e-mail: Ingo.Dirnstorfer@namlab.com

T. Mikolajick
e-mail: Thomas.Mikolajick@namlab.com

T. Mikolajick
Institute of Semiconductor and Microsystems, TU Dresden,
Nöthnitzer Strasse 64, 01187 Dresden, Germany

T. Mikolajick
Center for Advancing Electronics Dresden (cfaed), TU Dresden,
01062 Dresden, Germany

Q. Li (ed.), *Nanomaterials for Sustainable Energy*,
NanoScience and Technology, DOI 10.1007/978-3-319-32023-6_2

2.1 Dielectric Nanomaterials in Today's and Future Silicon Solar Cells

The introduction of dielectric nanomaterials was one of the major advances in silicon solar cell development. Thermal oxidation of the Si wafer resulted in a substantial improvement of the surface passivation quality and this improvement was essential for the first solar cells surpassing the 20 % efficiency mark in the 1980s [1, 2]. SiO_2 effectively suppresses surface recombination of photo-generated electron hole pairs. Additionally, SiO_2 provides excellent optical properties for controlling light reflection losses in the solar cell. In the subsequent years, additional dielectric nanomaterials emerged for solar cell passivation and these materials gradually developed from lab scale to industrial standard. SiO_2 is still used for high performance solar cells [3]. However, SiN_x:H became the most common dielectric material in solar cell manufacturing [4, 5]. Recently, Al_2O_3 also proved excellent passivation performance and established itself as an additional dielectric material in silicon solar cells [6, 7].

Figure 2.1a sketches a passivated emitter and rear cell (PERC), which is currently implemented in industrial manufacturing. The PERC concept is anticipated to become the dominant commercial cell technology by 2020 [8]. In the PERC solar cell, the front and rear sides are passivated with dielectric nanomaterials [9]. In most concepts, SiN_x:H is used to passivate the front side of the cell, whereas Al_2O_3 in combination with a SiN_x:H capping layer is applied at the rear side.

Since dielectric materials are insulators, the passivation layers are locally opened to facilitate the electrical contact between silicon and metallization. The state-of-the-art technology for contacting through the SiN_x:H layer is the application of a screen printing paste containing a lead borosilicate glass frit. During fast firing annealing at temperatures around 800 °C, this frit etches SiN_x:H and promotes the electrical contact between the front side metal paste and the Si surface [9]. The rear side metallization is contacted by local contact opening (LCO) [10] or laser fired contacts (LFC) [9]. These processes locally contact the Si wafer though point contacts, while the surface passivation layer is maintained in large parts.

Today's PERC solar cells benefit from considerable R&D effort during the last decades resulting in dielectric nanomaterials with excellent performance, stability and scalability in industrial environment. However, solar cell development moves forward and novel solar cell concepts emerge with higher conversion efficiencies and lower manufacturing costs. Selected cell concepts are displayed in Fig. 2.1(b–f). These novel concepts demand for advanced dielectric nanomaterials, which will be discussed in the following.

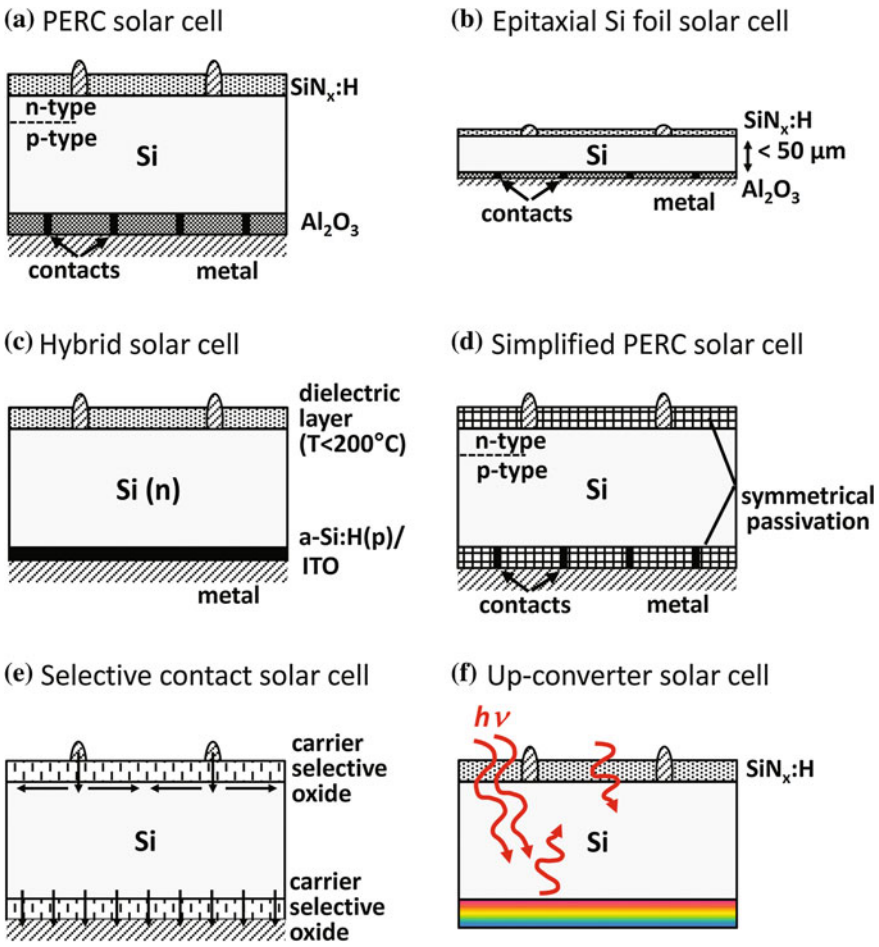

Fig. 2.1 Schematic drawing of the state-of-the-art PERC solar cell (**a**) and emerging solar cell concepts, which require further development of dielectric nanomaterials: epitaxial Si foil-based solar cell (**b**), hybrid silicon heterojunction solar cell with dielectric surface passivation (**c**), simplified PERC solar cell with symmetrical passivation (**d**), selective contact solar cell (**e**) and up-converter solar cell (**f**). The concepts are discussed in the text

2.1.1 Epitaxial Si Foil-Based Solar Cell

Thin, epitaxial crystalline Si foil-based solar cells are realized by CVD growth on porosified substrates. After deposition, the Si films are detached from the parent wafer and bonded to a foreign carrier, while the parent wafer is re-used [11]. A PERC-like epitaxial Si foil solar cell is shown in Fig. 2.1b. Epitaxial silicon solar cells with sub-50 µm absorber layers reach efficiencies of about 20 % today [12–14]. Thinning of Si absorbers is a very promising route to reduce material

consumption. Additionally, wafer thinning is motivated by conversion efficiency enhancement because the intrinsic solar cell efficiency limit imposed by Auger recombination shifts towards higher values when the wafer thickness is decreased from today's standard (∼180 µm) to values below 100 µm [15]. However, in thinned silicon absorbers, surface recombination losses and incomplete light absorption arise as critical limitations [16, 17], imposing higher requirements on the dielectric nanomaterials in the solar cells. The critical parameters for electrical and optical losses are discussed in Sects. 2.2 and 2.5, respectively.

2.1.2 Heterojunction Solar Cell with Dielectric Front Side Layer

Silicon heterojunction solar cells are based on a *pn*-junction with hydrogenated amorphous Si (a-Si:H) and crystalline Si (c-Si). Due to the very good surface passivation of a-Si:H, this cell concept reaches very high open circuit voltages (up to 750 mV) and efficiencies up to 24.7 % in double sided contacted cells [18]. Though excellent efficiencies are achieved, the short circuit current is limited by the very low quantum efficiency of the front side layers, i.e. a-Si:H and ITO, due to their poor photoelectric properties. To reduce the parasitic light absorption in these layers, hybrid solar cells are suggested. In hybrid solar cells, the *pn*-junction is located at the rear side and a highly transparent dielectric material is used at the front side (Fig. 2.1c) [19–21]. One obstacle for this concept is the low temperature budget of a-Si:H (T < 200 °C) [22] compared to the relatively high thermal activation energy required for the dielectric passivation layers (T ∼ 400 °C). The integration of hybrid SHJ solar cells with dielectric front side layers can be facilitated if the temperature budget of the dielectric passivation layer is reduced. Low-thermal budget processes are discussed in Sect. 2.3.4.

2.1.3 Solar Cell with Symmetrical Passivation

The state-of-the-art PERC concept is realized with two different passivation materials for the front and rear side, respectively. Two different materials are required, since charged dielectric passivation layers perform best on substrates with oppositely charged majority carriers [23–25]. In a simplified PERC process flow, the same passivation material is deposited in a single process step on both sides of the solar cell. A solar cell with symmetrical passivation materials for *p*- and *n*-type Si is shown in Fig. 2.1d. Symmetrical passivation is also applied in interdigitated back contact (IBC) solar cells for the *p*- and *n*-doped areas at the rear side [26, 27]. Symmetrical passivation can be realized by materials, which are free of intrinsic charges. Zero-fixed-charge multi-oxide nanolaminates are discussed in Sect. 2.4.1.

2.1.4 Solar Cell with Carrier Selective Contacts

PERC solar cells employ insulating dielectric passivation layers with local interconnects between silicon and metallization. Though necessary for the electrical contact, the metal-semiconductor interconnects partly degrade the solar cell performance, because of their high density of interface states and a very high local surface recombination rate. Therefore, the contact area requires thorough optimization to achieve both low recombination and ohmic losses [10]. An alternative to local point contacts are full area, carrier selective contacts, which provide a high level of surface passivation and electrical conductivity (Fig. 2.1e). In general, these contacts separate the absorber material, i.e. Si, and the metal contact by a medium with different conductivities for majority and minority carriers [28]. Dielectric passivation layers can be applied as carrier selective contacts if they provide sufficient electrical conductivity in addition to high surface passivation. Multi-oxide nanolaminates employing only dielectric materials are very interesting candidates due to their synergies with materials already used in PERC manufacturing. Dielectric carrier selective contacts are discussed in Sect. 2.4.2.

2.1.5 Up-Converter Solar Cell

In single junction solar cells, the dominant loss processes are sub-band gap transmission and thermalization losses of electron-hole pairs generated by photons exceeding the band gap energy. These losses can be significantly reduced if the solar spectrum is matched to the silicon band gap [29]. Figure 2.1f shows a solar cell concept with an up-conversion layer attached to the rear side. Within this layer two sub-band gap photons are up-converted into one photon, which can be absorbed in Si. As the up-conversion process utilizes sub-band gap photons, this process overcomes the fundamental Shockley-Queisser efficiency limit of 30 % [30]. Up-conversion shifts the theoretical efficiency limit of a single junction Si solar cell towards 40 % [31]. In a similar way, down-conversion converts high energy photons into two or more photons of lower energies. Down-conversion also shifts the efficiency limit due to the better utilization of the photon energy. Concepts for spectral conversion are discussed in Sect. 1.5.3.

2.2 Theory of Surface Recombination and Surface Passivation

2.2.1 Surface Recombination Model

Open bonds at the surface of a crystal result in additional energy levels, which could be located within the band gap and form recombination centers for electrons and holes. Free carriers are first captured in these deep traps and then recombine in a second step. The liberated energy is converted to lattice vibrations and phonons. The Shockley-Read-Hall (SRH) model describes the recombination rate U_{SRH} via deep traps by [32–34]:

$$U_{\mathrm{SRH}} = \sigma_n \sigma_p v_{\mathrm{th}} \left(n_s p_s - n_i^2\right) \int \frac{D_{it} dE}{\sigma_n (n_s + n_1) + \sigma_p (p_s + p_1)} \approx \frac{N_T v_{th} \sigma_n \sigma_p n_s p_s}{\sigma_n n_s + \sigma_p p_s} \quad (2.1)$$

with the thermal velocity v_{th} and the electron and hole concentrations n_{s} and p_{s} at the surface (unit: cm^{-3}). The free carrier concentrations are a function of substrate doping and the excess carrier concentration, which depends on the optical generation rate in an illuminated Si wafer. Furthermore, n_1 and p_1 are defined as

$$n_1 = n_i \exp\left(\frac{E - E_i}{kT}\right) \text{ and } p_1 = n_i \exp\left(-\frac{E - E_i}{kT}\right) \quad (2.2)$$

with the intrinsic carrier concentration n_{i} and the intrinsic energy level E_{i}. The surface traps are characterized by their density D_{it} (unit: eV^{-1} cm^{-2}) and the capture cross sections σ_{n} and σ_{p} for electron and holes, respectively. In general, trap levels are distributed throughout the band gap and their densities and capture cross sections are functions of trap energy. Therefore, the recombination rate is determined by an integral from the conduction to valence band energy level.

The SRH formula simplifies when assuming relevant illumination (n_{s}, $p_{\mathrm{s}} \gg n_{\mathrm{i}}$) and solely mid-gap defects at E_{i}. Under these assumptions the recombination rate only depends on the defect density N_{T} (unit: cm^{-2}), the free carrier concentrations at the surface and the capture cross sections of the defect (2.1). In this simplified formula the surface recombination is a linear function of N_{T}. When differentiating this expression with respect to the carrier concentration, a maximum is found at $p_{\mathrm{s}}/n_{\mathrm{s}} = \sigma_{\mathrm{n}}/\sigma_{\mathrm{p}}$, i.e. the highest recombination rate is reached when the ratio of holes and electrons is equal to the inverse ratio of their capture cross sections. The capture cross section ratio of mid-gap surface defects is asymmetrical. Typical $\sigma_{\mathrm{n}}/\sigma_{\mathrm{p}}$-values of Si surface defects are 1000 [23] and 20–1000 [35–37], when the surface is passivated with SiO_2 and Al_2O_3, respectively. Consequently, the highest recombination occurs when the surface concentration of holes exceeds the concentration of electrons.

The quality of the surface passivation is measured by the surface recombination velocity, which is defined as [34]

$$S_{\text{eff}} = \frac{U_{\text{SRH}}}{\Delta n} \tag{2.3}$$

with the injection level Δn. At a planar surface, the upper limit of surface recombination velocity is constituted by the thermal velocity of free carriers in the order of 10^7 cm/s [38]. In today's PERC solar cells, S_{eff} is typically below 100 cm/s [7, 39]. Very low surface recombination velocities in the range of 1 cm/s and even below are achieved with high quality SiO_2 [24], Al_2O_3 [7, 40] and SiN_x:H [41] passivation layers.

The surface recombination velocity is usually not measured directly but deduced from the effective carrier lifetime (τ_{eff}) in a Si substrate. Several mature techniques are available to determine the carrier lifetime in Si, such as quasi-steady-state photoconductance (QSSPC) [42, 43] microwave-detected photoconductivity (MDP) [44] or photoluminescence [45]. In a both side passivated Si wafer, the correlation between carrier lifetime and surface recombination velocity is [46]:

$$\frac{1}{\tau_{\text{eff}}} = \frac{1}{\tau_{\text{bulk}}} + \frac{2S_{\text{eff}}}{W} \tag{2.4}$$

with the wafer thickness W and the carrier lifetime of the bulk material τ_{bulk}. When the surface is poorly passivated and recombination rate becomes very high, an additional term describing the minority carrier diffusion towards the surface has to be taken into account [46]. The measured effective carrier lifetime is a function of surface and bulk recombination and both recombination channels cannot be separated with this measurement. Therefore, the evaluation of passivation materials is usually done on high quality float zone (fz) Si substrates. In fz Si wafers, the impurity concentration is very low and SRH recombination at bulk defects is negligible. The bulk lifetime is only limited by Auger and radiative recombination, where the excess energy is transferred to a free carrier or a photon. The recombination rate of these intrinsic processes depends on doping concentrations and injection level [47]. Considering a typical injection level of non-concentrating solar cells ($\Delta n = 10^{14}$ cm^{-3}) and a typical substrate resistivity of 2 Ωcm, the intrinsic carrier lifetime can be calculated to be 15 and 25 ms for p- and n-type Si, respectively. When the measured effective carrier lifetime is well below the calculated intrinsic limit, (2.4) simplifies to $S_{\text{eff}} \approx 0.5\ W/\tau_{\text{eff}}$. Based on this reasoning the measured carrier lifetime is commonly used as a measure for the surface passivation quality.

2.2.2 *Dielectric Charges and Near Surface Recombination*

According to (2.1), the surface SRH recombination is a function of the electron and hole concentrations at the surface. These concentrations are strongly influenced by a dielectric surface passivation layer if it contains intrinsic fixed charges. A dielectric layer with positive fixed charges attracts electrons, whereas a negatively charged

layer attracts holes to the Si surface. The surface charge densities can be calculated by simultaneously solving the Poisson and continuity equations with the boundary conditions given by surface SRH recombination and optical generation. A numerical scheme for solving these equations was described by Girisch et al. [48]. Nowadays, fast calculation of carrier distributions and recombination rates is provided by several shareware Poisson solvers, such as PC1D [49] or AFORS-HET [50].

Figure 2.2a shows the simulated electron and hole surface concentrations as a function of the fixed charges density (Q_f). Densities are always positive; however, Q_f often ranges from negative to positive values, indicating the polarity of the charges. Fixed charges with densities in the order of 10^{12} cm^{-2} can heavily influence the surface carrier concentration. When the wafer is illuminated, the surface minority carrier concentration strongly increases whereas the relative change of majority carriers is small. As a consequence, the asymmetry in free carrier concentrations reduces with increasing optical generation. However, this asymmetry is still sufficient to effectively suppress surface recombination.

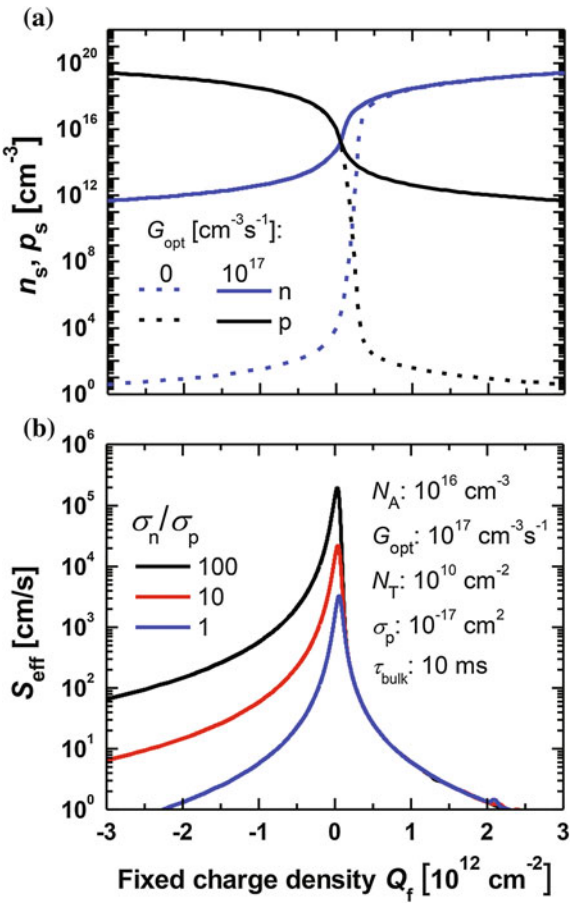

Fig. 2.2 AFORS-HET simulation of surface electron and hole concentrations with and without illumination (**a**) and surface recombination velocity (**b**) as a function of the fixed charge density in the dielectric. The input parameters for the simulation are displayed in the figure. Both, negative and positive fixed charges suppress surface recombination

The effect of fixed charges on the surface recombination is shown in Fig. 2.2b. For simulation, a constant generation rate is used as input parameter, e.g. caused by sun light illumination. The injection level is not constant as it depends on the effective carrier lifetime via $\Delta n = G_{opt}/\tau_{eff}$ and thus on variable surface recombination. The highest recombination is found at the point where the fixed charges result in $p_s/n_s = \sigma_n/\sigma_p$. A deviation from this condition reduces the surface recombination as the recombination becomes limited by either holes or electrons. Consequently, negative and positive fixed charges suppress surface recombination equally. At low injection conditions the relation between surface recombination velocity and fixed charges can be expressed analytically [51, 52]:

$$S_{eff} \sim \frac{N_{dop}}{Q_f^2} \tag{2.5}$$

with N_{dop} being the acceptor or donor concentration in *p*- or *n*-type Si, respectively. When the σ_n/σ_p-ratio increases, the recombination maximum slightly shifts towards higher surface hole concentrations, i.e. towards negative fixed charges. However, this shift is very small. More significant is the fact that the surface recombination curve becomes asymmetrical due to the higher capture rate for one carrier type.

The influence of charge polarity on the Si surface band bending is shown in Fig. 2.3. In *p*-type Si, negative fixed charges create an accumulation layer, where majority carriers are accumulated at the surface. Positive fixed charges form in inversion layer with increased minority carrier concentration. Both charge polarities suppress surface recombination as shown in Fig. 2.2. However, an additional near surface recombination (NSR) channel opens in the inversion layer. At a distinct point within the inversion layer, the carrier concentrations fulfill the requirement for highest recombination rate, i.e. $p_s/n_s = \sigma_n/\sigma_p$. For typical solar cell doping concentrations ($\sim 10^{16}$ cm^{-3}) and fixed charge densities ($\sim 10^{12}$ cm^{-2}), this point is approximately 100 nm below the surface. At this position, the recombination at deep

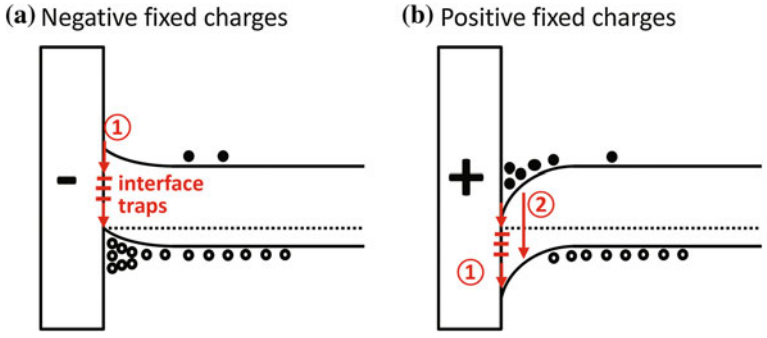

Fig. 2.3 Schematic band diagram of *p*-type Si with a passivation layer containing negative (**a**) and positive (**b**) fixed charges. *Arrows* indicate the recombination channels through interface traps at the surface (*1*) and in the near surface region (*2*)

bulk defects is strongly enhanced. This effect was first observed with positively charged SiO_2 [23–25] and SiN_x:H [53, 54] passivation layers on *p*-type Si. Later, this effect was also measured with negatively charged Al_2O_3 passivation layers on *n*-type Si [40, 55]. The effect was analytically described for the first time by Glunz et al. using an empirical formula, which was deduced from the ideal diode equation [56]:

$$S_{\mathrm{NSR}} = \frac{J_0}{q\Delta n}\left(\sqrt{\Delta n / n_{0,\,\mathrm{min}} + 1} - 1\right) \tag{2.6}$$

with the equilibrium minority carrier concentration $n_{0,\mathrm{min}}$ and the saturation current J_0 as fit parameter. In this equation, the near surface recombination velocity S_{NSR} increases with decreasing Δn. Consequently, this effect dominates the lifetime at low injection levels. Though the near surface recombination was described already more than one decade ago, the origin of the involved recombination centers is still under discussion. Steingrube et al. suggested the existence of a surface damage region containing additional defects, which are potentially formed by hydrogen incorporation during the deposition of the dielectric layer or the post-deposition annealing step [51, 57–59]. Alternatively, it was shown that homogenously distributed bulk defects could significantly contribute to near surface recombination even if their concentration is very small. In the inversion region of p-type Si, "harmless" bulk defects turn into highly efficient recombination centers when their σ_n/σ_p–ratio is large and the energy level of the defect is located in the lower half of the band gap [60]. The reduced lifetime in the low injection level range can also be consistently explained by transport of carriers towards recombination centers at the edge of the sample [61, 62].

Figure 2.4 shows the effective carrier lifetime in *p*- and *n*-type Si with an ideally passivated surface ($S_{\mathrm{eff}} = 0$). A passivation layer with negative fixed charges is assumed resulting in an inversion layer in *n*-type Si. The carrier lifetime is limited

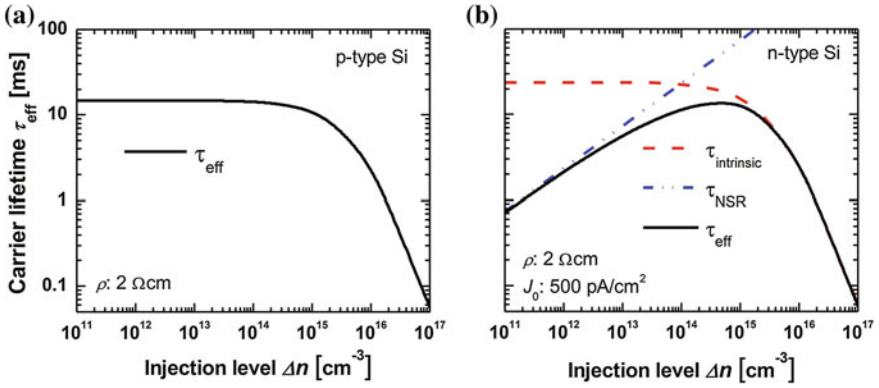

Fig. 2.4 Calculated carrier lifetime as a function of injection level for *p*- (**a**) and *n*-type (**b**) Si. A passivation layer with negative fixed charges is assumed ($S_{\mathrm{eff}} = 0$). The intrinsic bulk lifetime ($\tau_{\mathrm{intrinsic}}$) and near surface recombination are calculated according to [47] and (2.6)

by the intrinsic bulk lifetime and, in *n*-type Si, also by the near surface recombination. In the injection level range of 10^{13}–10^{14} cm^{-3}, which is typical in non-concentrator solar cells, the near surface recombination constitutes a critical limitation for carrier lifetime. As a consequence, *p*/*n*-type Si is usually combined with negatively/positively charged passivation layers.

2.2.3 Surface Passivation

Dielectric nanomaterials provide chemical and field-effect passivation. Chemical passivation reduces surface recombination centers and results in low D_{it} values. Field-effect passivation is caused by intrinsic charges in the dielectric layer, which produce an electric field altering the electron and hole concentrations at the surface. These two passivation effects control the key parameters of the SRH surface recombination process (2.1).

2.2.3.1 Chemical Passivation

The termination of a regular crystalline lattice results in a large number of unsaturated chemical bonds at the surface. For Si, thermal surface oxidation provides a very effective saturation of chemical bonds resulting in a low density of interface states. The high electrical quality of the Si/SiO_2 interface is one of the key advantage of Si as a semiconductor [63]. Deal and Grove studied the thermal oxidation kinetics of Si in detail. Based on their model, oxygen diffuses from the gas phase through the amorphous oxide towards the substrate where it reacts with silicon to SiO_2. The oxide formation occurs at an buried interface [64, 65]. Despite of a significant bond density mismatch of crystalline Si and amorphous SiO_2, the interface was found to be rather abrupt within very few atomic monolayers. Within this interface the Si atoms are either bound in Si or in SiO_2 leaving a very low density of open bonds [66].

When high-*k* oxides, such as Al_2O_3, TiO_2 or HfO_2, are deposited on Si, the interface is not abrupt but the materials are separated by an interfacial SiO_x layer [63]. The interfacial SiO_x layer thickness is usually in the order of a few monolayers [52, 67]. This layer is formed during the oxide deposition process and it is even found on H-terminated substrates where the native SiO_2 layer was removed by HF etching prior to deposition [40]. However, the SiO_x interface thickness increases when deposition is done on substrates covered by native SiO_2 [68]. Very thick interfacial SiO_x layers of up to 8 nm were found in samples produced by reactive sputtering of Al_2O_3 [69]. The SiO_x thickness also slightly increases during post-deposition annealing at 400 °C [40, 70]. It is suggested that residual –OH groups react with the Si surface [71]. Interfacial SiO_x is also found in HfO_2 passivation layers [72, 73]. In SiN_x:H, a thin SiN_xO_y layer is found at the interface to silicon. This oxynitride is suggested to be formed in a reaction with native SiO_2

during SiN_x:H deposition [74]. As a consequence, the interfaces between Si and the passivation layers are basically Si/SiO_2-like. The high electrical quality of interfacial SiO_x is suggested to be the key to the excellent chemical passivation of dielectric materials [52, 75].

The surface passivation is significantly enhanced by hydrogenation of the Si/SiO_x interface. Most dielectrics used for surface passivation already contain a high quantity of hydrogen, as hydrogen is part of the deposition chemistry. Typical Al_2O_3 passivation layers contain 2–7.5 at.% hydrogen, mainly incorporated as –OH groups [70], with increasing concentration at lower deposition temperatures [76, 77]. In SiN_x:H, the hydrogen concentration is in the range of 10 and 20 at.% [41, 78]. SiO_2 contains about 8 at.% of hydrogen [79] when grown by ALD, whereas SiO_2 grown by thermal oxidation of Si is free of hydrogen.

Hydrogenation of the interface is a temperature activated process, which involves the transport of hydrogen towards the interface and the reaction with open bonds at the Si surface. The elevated hydrogen concentration at the Si/SiO_x interface after annealing can be detected with SIMS measurements [80]. The dynamics of this process depends on the annealing temperature and the microstructure of the dielectric layer [81, 82].

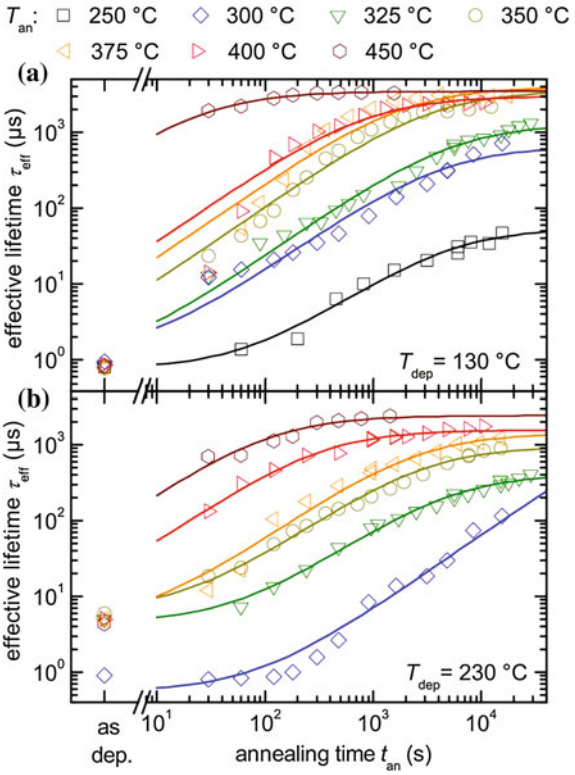

Fig. 2.5 Effective carrier lifetimes (at $\Delta n = 10^{15}$ cm^{-3}) as a function of cumulative annealing time t_{an} and annealing temperature T_{an} (in N_2 atmosphere). The deposition temperatures T_{dep} of the Al_2O_3 passivation layers are 130 °C (**a**) and 230 °C (**b**). The "as dep." annealing time refers to the as-grown layer. The *solid lines* are fits using (2.7). Reprinted with permission from Applied Physics Letters **104**, 061606. Copyright 2014, AIP Publishing LLC [82]

Figure 2.5 shows the activation dynamics of an Al_2O_3 layer. The activation of the passivation layer ($\tau_{eff} > 1$ ms) requires an annealing temperature between 350 and 450 °C and an annealing time of about 10 min. The evolution of carrier lifetime as a function of the annealing time t_{an} is described by [82]:

$$\frac{1}{\tau_{eff}(t_{an})} = \frac{1}{\tau_{bulk}} + \frac{2}{W}\left(S_\infty + \frac{S_0}{1 + R_{act} t_{an}}\right) \tag{2.7}$$

$$R_{act} = C \cdot \exp\left(-\frac{E_A}{k_B T_{an}}\right) \tag{2.8}$$

with S_0 and S_∞ being the surface recombination velocities prior to and after long-time annealing, respectively. These two parameters and the reaction rate R_{act} were fitted to the experimental data and it was found that the reaction rate exhibits Arrhenius behavior described by (2.8). Thus, the hydrogenation of interface defects is a temperature activated process with a characteristic activation energy. Though the applied fit functions varied in different investigations, similar activation energies of 1.5–1.6 eV [82] and 0.9–1.2 eV [81] were found for ALD-grown Al_2O_3 and SiO_2/Al_2O_3 layers after annealing in N_2 atmosphere. PVD-grown Al_2O_3 has an activation energy of 1.1 eV during H_2/N_2 annealing. In PVD-grown layers, the reaction rate is about four orders of magnitude lower due to a lack of mobile atomic hydrogen [83]. For thermally grown SiO_2, values of 1.5–1.7 eV are measured during annealing in H_2 atmosphere [84]. Since the activation energies of different materials match very well and exceed the activation energies reported for hydrogen diffusion, it is concluded that hydrogenation of the interface is a reaction limited process [81, 82, 84, 85].

Layers with high hydrogen content can be activated without external hydrogen source. For activation of Al_2O_3, a simple hot plate annealing in lab environment is virtually sufficient. The application of H_2-containing atmospheres hardly improves the passivation level of Al_2O_3 [81, 86] and TiO_2 [87]. Therefore, most groups perform annealing in a temperature controlled oven with N_2 atmosphere. However, annealing in H_2-containing gas atmosphere is required for passivation layers with low or zero H-content, such as Al_2O_3 deposited by PVD [83] or thermally grown SiO_2 [84].

The reaction rate is also influenced by the microstructure of the material, i.e. the structural material properties determine the constant C in (2.8). Figure 2.5 shows that activation of Al_2O_3 is significantly faster when the layer is grown at lower deposition temperatures. At low ALD and PECVD process temperatures, the mass density of films reduces due to enhanced incorporation of carbon and hydrogen contaminations [70, 76, 77]. The larger hydrogen reservoir supports accelerated hydrogenation during post-deposition annealing [81, 82].

Annealing supports hydrogenation of the interface, however, at the same time it also leads to outdiffusion and hydrogen loss. When the outdiffusion process prevails, the level of passivation degrades. This degradation is observed when the Al_2O_3 layer thickness descends below a value of about 10 nm (Fig. 2.6a). The reduction of carrier lifetime is correlated to a strong increase of D_{it} values (Fig. 2.6b), which is consistent with the creation of dangling bonds due to hydrogen release [67, 88].

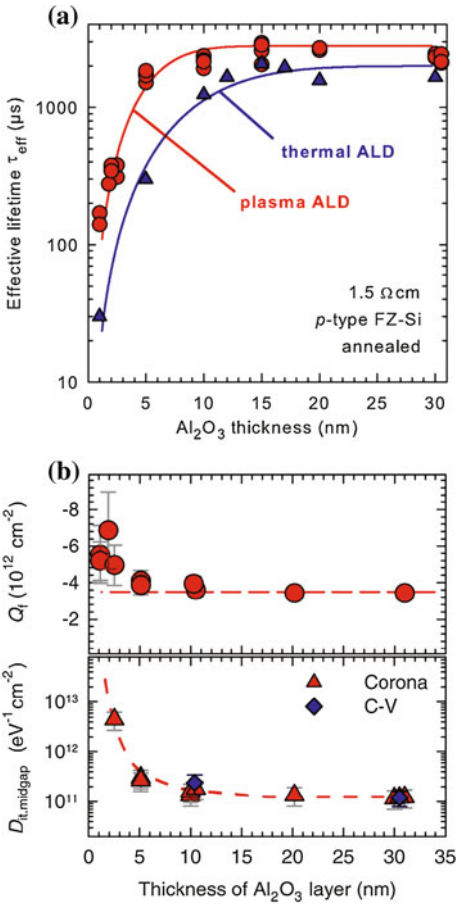

Fig. 2.6 Effective carrier lifetime (**a**) and Q_f and D_{it} values (**b**) as a function of Al_2O_3 layer thickness after annealing at 425 °C. At a layer thickness below of 10 nm, the carrier lifetime drops due to increased D_{it} values. Reprinted with permission from Journal of Applied Physics, **109**, 113701. Copyright 2011, AIP Publishing LLC [67]

The loss of hydrogen becomes more critical at higher annealing temperatures. In thermal effusion experiments on ALD-grown Al_2O_3, the hydrogen signal significantly rose at temperatures above 400 °C [81]. The peak temperature of H_2 and H_2O effusion depends on the microstructure of the films. Films deposited at temperatures between 200 and 400 °C are relatively dense and the maximum effusion shifts towards 700 °C, whereas the effusion maximum already appears at 400 °C when the films are grown at only 50 °C. Thus, denser films provide better stability against hydrogen loss during high temperature annealing [81]. Furthermore, higher layer thickness provides better temperature stability [89]. Hydrogen loss and film degradation is also observed in SiN_x:H films at temperatures above 500 °C [78].

Temperature stability of passivation layers is crucial as the PERC process sequence contains a short-term fast firing step at 800–900 °C. To increase the firing stability of thin Al_2O_3 layers, the films are usually capped with a thick ($\sim$100 nm), hydrogen-containing SiN_x:H layer [89–91]. Nuclear reaction analysis measurements confirm that this capping prevents H outdiffusion and maintains a high

hydrogen concentration at the interface [92] resulting in a high chemical passivation after firing.

The available bonds per unit area of an unpassivated Si surface depend on the crystal orientation. In the Si (111) plane, the available bond density equals 1.2×10^{15} cm^{-2}, whereas the density is only 7×10^{14} cm^{-2} in the (100) plane [93]. After thermal oxidation of the surface, the available bond density at the silicon surface is found to correlate to the interface state density. As interface states below the gate dielectric are critical for the transistor functionally, todays CMOS manufacturing is based on (100) substrates [65].

The surface plane orientation is more complex in solar cells. Standard mono-crystalline solar cells are produced on (100) wafers where at least the front surface is textured and the surface plane orientations become (111). However, several studies revealed that the correlation between surface plane orientation and surface recombination is low. Texturing is found to increase the emitter saturation current density with a textured-to-planar ratio of 1.5–2. However, the degradation was mainly attributed to the larger surface area whereas the influence of the crystal orientation was small [94]. Liang et al. investigated the Al_2O_3 passivation of different surface orientations and measured a better passivation of the (100) surface, however, the improvement was correlated to an increase in fixed charges rather than a reduction of interface defects [95]. Black et al. also reported an influence of the different surface orientations on the performance of as-grown Al_2O_3 layers. However, the differences vanished after annealing [96]. On multi-crystalline wafers with well-passivated surfaces, the carrier lifetime was limited by recombination through crystal defects and the influence of surface planes orientation was negligable [97].

2.2.3.2 Field-Effect Passivation

Most dielectric layers contain intrinsic fixed charges, which provide field-effect passivation. Two methods are commonly applied to determine the fixed charge densities, the capacitance-voltage (CV) measurement on a metal-insulator-semiconductor test structure [34, 93] and the corona charge measurement directly applied on the passivated substrate [52, 56]. Additionally, lateral 2D mapping of the fixed charge distribution was demonstrated using a passivated substrate with a full area rear side electrode and photoluminescence imaging [98] or carrier lifetime mapping [99, 100]. Figure 2.7 shows a corona charge measurement on three different passivation materials. In this measurement the surface recombination velocity peaks when the deposited corona charges compensate the field-effect passivation. The measurement reveals positive fixed charges in SiN_x:H and SiO_2 layers and negative charges in Al_2O_3.

Fixed charges are formed during film deposition and during post-deposition annealing. In SiN_x:H, the intrinsic charges are related to K centers ($\bullet Si \equiv N_3$), which are formed by Si atoms backbonded to nitrogen [101]. With increasing [N]/[Si] ratio, the density of K centers increases at the interface, although these

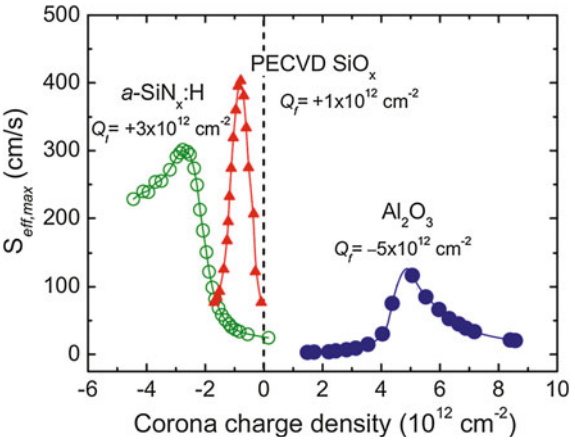

Fig. 2.7 Surface recombination velocity versus deposited corona charge density for SiN_x:H, SiO_2 and Al_2O_3 layers after annealing at 400 °C. Reprinted with permission from Journal of Vacuum Science & Technology A, **30**, 040802. Copyright 2012, American Vacuum Society [6]

centers are to some extent passivated by the presence of H [102]. These centers have amphoteric character with a positive, neutral or negative charge state. In stoichiometric and N-rich SiN_x:H films, the dangling bond of the K center is the dominant deep defect level, which becomes positively charged after electron emission. When the [N]/[Si] ratio is reduced, the density of K centers decreases and the films converge to amorphous Si, which is free of intrinsic charges [41, 103, 104].

In Al_2O_3, the fixed charge density depends on the applied process parameters during layer deposition. Plasma enhanced deposition methods tend to produce higher fixed charge densities than thermal processes [105–107], presumably due to the influence of highly reactive gas species in the plasma. Post-deposition annealing further supports the fixed charge formation and the charge density increases with annealing temperature up to about 500 °C [86, 108]. At higher annealing temperatures, the effect on charge formation reverses and charge densities decrease.

Oxide fixed charges are located at the interface to Si. When the Al_2O_3 thickness is reduced to 1 nm the fixed charge density hardly changes [67, 88] (Fig. 2.6b). This result is confirmed by CV-measurements on slant-etched oxides (Fig. 2.8). For these measurements, ALD-grown Al_2O_3 and SiO_2 layers are capped with an insulating HfO_2 top layer to block the leakage current even in very thin oxides. With this strategy it is possible to measure the flat band voltage of oxides as a function of thickness down to the sub-nanometer range [109]. The measured flat band voltage linearly increases with the effective oxide thickness (EOT), which suggests an oxide with solely interface charges [34, 93]. The densities are 2×10^{11}, 3×10^{12} (negative charges) and 1×10^{12} cm^{-2} (positive charges) in HfO_2, Al_2O_3 and SiO_2, respectively. A significant deviation from the linear function only appears when EOT approaches the value of the capping layer (about 8 nm EOT), i.e. the oxide thickness falls below 1 nm (grey line in Fig. 2.8). For Al_2O_3, a steep V_{fb} drop of about 1 V appears at an Al_2O_3 thickness below 1 nm. In the SiO_2 layer,

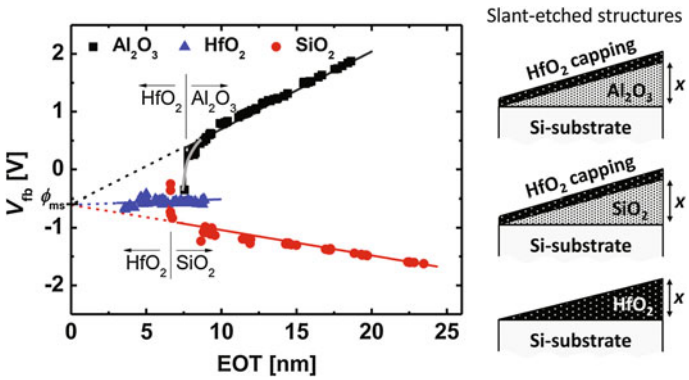

Fig. 2.8 Flat band voltages as a function of EOT determined on slant-etched Al_2O_3 and SiO_2 layers with HfO_2 capping and on slant-etched HfO_2 (stacks plotted on *right side*). The data follow a linear function (*solid lines*) down to sub-nanometer Al_2O_3 and SiO_2 layers (capping layer EOT: ~8 nm). This linearity suggests that charges are located at the interface to Si. Reprinted with permission from ACS Appl. Mater. Interfaces, **7**, 28215–28222. Copyright 2015, American Chemical Society [109]

the voltage drop is less pronounced. The flat band voltage drop correlates to the built-up of fixed charges within the first nanometer of the layer.

Bulk charges would result in a parabolic dependency on EOT, which is not visible in Fig. 2.8. Based on the V_{fb} function and a measurement error of ±100 mV, the bulk charge density is below 2×10^{17} cm^{-3} in ALD-grown SiO_2 and Al_2O_3 [109]. Assuming an EOT of 20 nm, the influence of bulk charges on the flat band voltage is comparable to the effect of interface charges with a density of 2×10^9 cm^{-2}. This result indicates that the influence of bulk charges is negligible. However, earlier investigations on slant-etched Al_2O_3 layers indicated a significant density of negative [110] or positive [111, 112] bulk charges in the range of 10^{19} cm^{-3}. The large spread of values might be explained by the difficulty to exclude systematic error sources in the thickness series, such as charge trapping during CV measurements.

2.2.3.3 Formation of Fixed Charges in Al_2O_3

The origin of the interface charges in Al_2O_3 is still under discussion. It is found that Al_2O_3 has different structural properties at the interface to Si, where the fixed charges are located. In situ x-ray photon spectroscopy (XPS) revealed a strongly increased [O]/[Al] ratio at the interface to Si [67, 113]. Figure 2.9a shows the excess O fraction as a function of the layer thickness. At the interface, about 50 % of oxygen is neither stoichiometrically bound to Si as SiO_2 or to Al as Al_2O_3 [113]. When moving away from the interface, the O-excess rapidly drops and the [O]/[Al] ratio finally approaches the nominal value of 1.5. Post-deposition annealing at 400 °C only slightly affects the [O]/[Al] ratio suggesting that the O-rich layer is

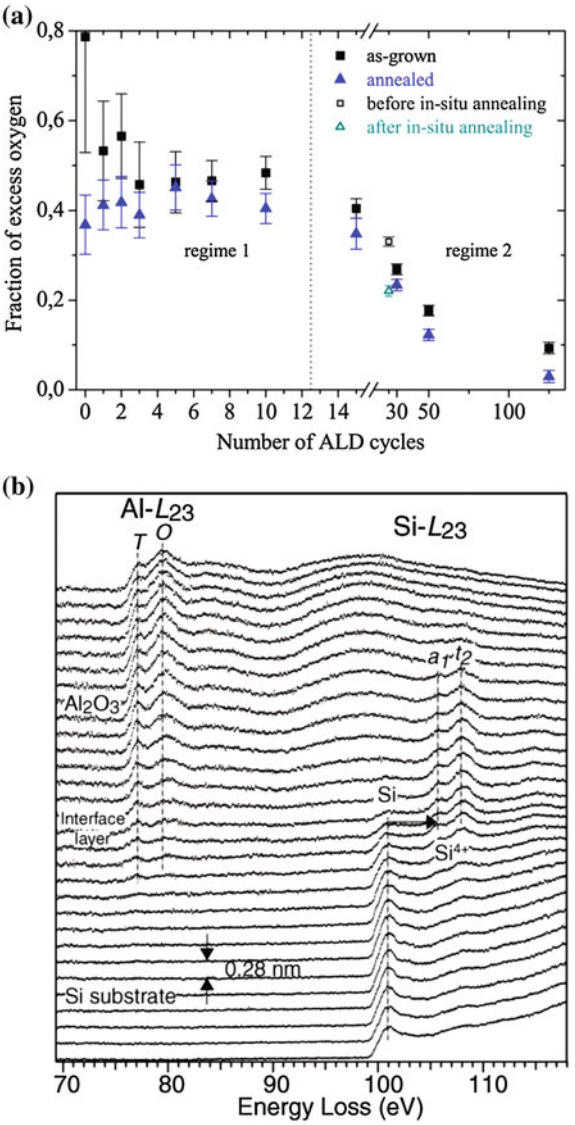

Fig. 2.9 XPS (**a**) and EELS (**b**) measurements of the initial growth region in Al_2O_3. XPS data reveal an O-excess, which decreases with increasing Al_2O_3 layer thickness. Reprinted with permission from J. Vac. Sci. Technol. A **30**, 04D106. Copyright 2012, American Vacuum Society [113]. Spatially resolved EELS data of a $Si/SiO_x/Al_2O_3$ cross-section show an enhanced tetrahedral coordination of Al atoms (Al-L_{23} T peak) close to the interface to Si. Reprinted with permission from Appl. Phys. Lett. **83**, 4306. Copyright 2003, AIP Publishing LLC [114]

already formed during layer deposition. Apparently, the stoichiometry deviation is caused by the initial growth of Al_2O_3 on the Si substrate.

Kimoto et al. investigated the Al coordination within Al_2O_3 by spatial resolved electron energy loss spectroscopy (EELS) [114]. Figure 2.9b shows the energy-loss near-edge structures (ELNES), which are sensitive to the valence and the coordination of the specific elements. The authors investigated the Al-L_{23} ELNES and found the T and O peaks throughout the layer, corresponding to tetrahedrally and octahedrally coordinated Al in Al_2O_3, respectively. However, the intensity of the T

peak, i.e. the tetrahedral coordination, is dominant near the interface. Additionally, it is found that the Si-L_{23} fine structure does not differ within the amorphous oxide layer at the interface. It is suggested that an aluminum silicate interface layer is formed, where Si atoms exist as SiO_4 tetrahedra. This tetrahedral coordination of cations in aluminum silicate influences the initial growth of Al_2O_3 resulting in different Al coordination at the interface compared to the bulk layer [114].

Lucovsky et al. investigated the local atomic structure in binary SiO_2–Al_2O_3 glasses and found that Al atoms were incorporated in both Al^{3+} ions and in $AlO^-_{2/4}$ tetrahedral groups due to the different electronegativity of the cations. The Al^{3+} ions are incorporated in a site, which has an octahedral coordination by oxygen atoms. Its positive charge is autocompensated by the negative charge of an $AlO^-_{2/4}$ network group. To ensure charge neutrality, the ratio of tetrahedral and octahedral Al-coordination is 3:1 [115]:

$$2Al_2O_3 \equiv 3AlO^-_{2/4} + Al^{3+} \tag{2.9}$$

As the $AlO^-_{2/4}$ network group is O-rich, an excess of tetrahedral coordination is consistent with the O-excess observed with XPS at the interface. Since the structural deviations spatially correlate to the location of fixed charges it is suggested that the tetrahedral coordination is the root cause for the negative charges in Al_2O_3 [6, 52]. Another approach for understanding the intrinsic charge formation is based on charged point defects. First principles calculations of defect formation energies reveal that oxygen interstitials (O_i) and aluminum vacancies (V_{Al}) have the lowest formation energies and are the most stable defects in O-rich crystalline Al_2O_3 [116]. Both defects are negatively charged and form energy levels close to the valence band of Si according to simulation. Therefore, O_i and V_{Al} point defects are suggested to act as fixed charge centers in crystalline Al_2O_3 [117, 118]. Al_2O_3 passivation layers are amorphous since crystallization does not occur at the applied process temperatures. Nevertheless, point defects are also suggested to be the origin for the negative charges in amorphous Al_2O_3 [113].

Charges in passivation layers are commonly referred to as ‘fixed’ charges. However, several studies indicate that the charge density at least partly depends on external forces such as illumination and electric field. Gielis et al. observed a continuous increase of charge density in Al_2O_3 after laser illumination during second harmonic generation measurements [119]. Liao et al. illuminated the Al_2O_3 passivation with sun light for several 100 h. During light soaking the carrier lifetime increased from 1 to 1.5 ms, which was correlated to an increase of negative charges in Al_2O_3 [120]. Illumination also reduces the density of positive charge in SiN_x:H films [54]. The authors explain this effect by a photo-induced electron injection into the dielectric. When the samples are stored at dark the charge injection at least partly reverses and the measured charge density returns to the initial value.

Charging of Al_2O_3 is also observed as hysteresis in CV measurements [68, 121, 122]. Hysteresis becomes visible when the charge density changes during the

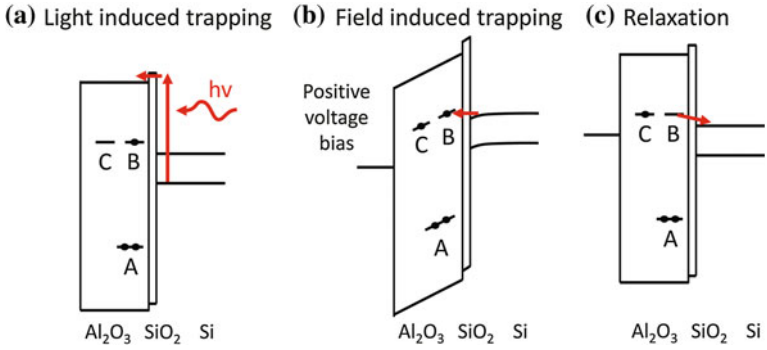

Fig. 2.10 Simplified energy diagram of Al_2O_3 to illustrate the role of fixed and trapped charges. Defect site A is negatively charged due to its low energy level. Defect sites B and C can trap electrons from Si during illumination (**a**) or application of electric field (**b**). After the external stress pulse, the electrons partly relax to the Si conduction band (**c**)

voltage sweep due to electron trapping at positive voltages and electron detrapping at negative voltages applied to the dielectric.

Figure 2.10 shows a simplified energy diagram of trap sites in Al_2O_3 to illustrate the difference between fixed and trapped charges. Structural defects create different energy levels in the Al_2O_3 band, which could interact with the Si substrate. Three different defect sites are distinguished as suggested in [123]. Defect site A is associated with a deep energy level, which is located close to the Si interface. Assuming an acceptor or amphoteric character of this defect, it will be intrinsically charged by electron capture from Si. Hence, this site is negatively charged and the charges are fixed due to the high activation energy. Defect site A could be related to tetrahedrally coordinated $AlO_{2/4}^{-}$ units or to other defects caused by oxygen excess. In crystalline Al_2O_3, intrinsic O_i and V_{Al} point defects are calculated to form deep traps with energy levels close to that of defect site A drawn in Fig. 2.10 [117, 118]. Similar structural defects might be responsible for deep electron traps in amorphous Al_2O_3.

Defect sites B and C are located above the Si Fermi level and charge trapping requires an external force such as illumination or electric field. Light absorption could lead to electron injection into the dielectric layer where the electrons are captured into trap sites (Fig. 2.10a). The application of an electric field lowers the trap level energy and the barrier height for electrons tunneling towards the defect (Fig. 2.10b). As soon as the layer returns in an unstressed state, i.e. light or electric field are switched off, the trapped charges tend to relax to the energetically favorable Si conduction band (Fig. 2.10c).

The dynamics of charge trapping and detrapping has been extensively investigated for nonvolatile memory devices [124–126]. Charge trapping is described by tunneling through the interfacial SiO_x layer into the high-k dielectric. As the tunneling probability depends on the energy barrier height and the tunneling distance [93], states close to the interface are occupied first. The same applies for detrapping via tunneling. States close to the interface relax the fastest. Using the simplified

drawings in Fig. 2.10, charges in defect site B have poor retention and relaxation quickly starts after the external stress is removed. This defect could cause hysteresis effects during measurements. Defect site C has higher retention and it remains charged due to the lower tunneling probability for trapped charges. If charges are trapped at this defect, the layer remains charged even after the external stress is removed. As the trapped charges have to pass through the interfacial SiO_x layer, the thickness of this layer essentially determines the tunneling probability. Consequently, the trapped charge density in Al_2O_3 reduces when this barrier is enforced by additional SiO_2 deposition [68, 127].

Trapping states in Al_2O_3 were characterized by the trap spectroscopy by charge injection and sensing (TSCIS) method [128, 129]. It was found that crystalline Al_2O_3 contains a rather narrow ($\sim$0.2 eV) trap band with a high density of trapping states. This band is located at 2.16 eV below the Al_2O_3 conduction band, which is roughly the energy position of defect sites B and C in Fig. 2.10. However, in amorphous Al_2O_3 with post-deposition annealing temperatures below 1000 °C, a homogeneous trap distribution was found [128]. Therefore, defects sites B and C are representatives of a continuous defect distribution in amorphous Al_2O_3 layers.

As trapped charges could significantly contribute to the field-effect passivation it was suggested to engineer their density. Werner et al. could increase the charge density up to 10^{13} cm^{-2} after applying an external positive voltage to a metal electrode on top of Al_2O_3. Unless the samples are annealed at 350 °C the charge retention is very good and the trapped charges support the field-effect passivation [123]. A substantial increase of trapped charges is achieved by Ti-doping of Al_2O_3, which also results in improved carrier lifetimes [122]. Charge trapping is also observed in SiN_x:H films, which are positively charged. The charge density could be increased above 10^{13} cm^{-2} after applying an external voltage [130]. The net charge polarity could also be turned from positive to negative after electron trapping in SiN_x:H films [131].

2.3 Deposition Methods

In solar cell manufacturing, plasma enhanced chemical vapor deposition (PECVD) is the dominant deposition technique for front and rear side passivation layers. Besides PECVD, only the atomic layer deposition (ALD) technique reached a significant market share of 10–20 % for processing the Al_2O_3 rear side passivation. Other methods have been developed as well. However, according to the ITRPV forecast of 2015 they are not expected to gain significant market share within the next decade [132].

2.3.1 Plasma Enhanced Chemical Vapor Deposition

PECVD is used to deposit thin films from the gas phase. A plasma generator produces a glow discharge (plasma) in which precursor gases are (partly)

transformed into radicals, ions or other highly excited species. These atomic and molecular species react with the substrate resulting in material deposition. Since the excitation of the precursor gases occurs by collision in the gas phase, the substrate can be maintained at low temperature. The low deposition temperature is one of the main advantages of PECVD over the conventional CVD process.

The film properties strongly depend on the deposition parameters and the reactor design [4, 5, 74]. Common reactor designs are parallel-plate ('direct' plasma) and 'remote' plasma systems. In parallel-plate reactors, the silicon wafer is placed between the two electrodes and is hence in direct contact with the plasma. In this configuration, the plasma frequency becomes a crucial parameter. To reduce the plasma damage by accelerated ions, high-frequency (>13.56 MHz) plasma systems are used [41, 78, 133]. In remote PECVD systems, the process gas is excited outside of the deposition chamber and the silicon wafer is not in direct contact with the plasma and ion bombardment damage is largely avoided. The widespread industrial high-throughput MAiA® system of Meyer Burger AG employs a 2.45 GHz linear microwave plasma source where a quartz tube with inner copper antennas generates the plasma outside of the tube [134].

Table 2.1 gives an overview of applied precursor gases and process conditions for PECVD of different passivation materials. For SiN_x:H deposition, ammonia and silane are commonly used. However, experiments were also done with additional N_2 and H_2 gas supply to grow layers close to ideal stoichiometry [78] and to enhance the hydrogen incorporation [41], respectively. The stoichiometry of SiN_x:H films can be widely adjusted by the ratio of precursor gases and this flexibility is used to tune the films for best performance. The [Si]/[N]-ratio controls the refractive index and absorption coefficient, which determine the antireflection properties of the SiN_x:H layer (Sect. 2.5.1). Additionally, the surface passivation properties depend on stoichiometry, whereby a general trend towards better performance is found in more Si-rich SiN_x:H films [41, 134, 135]. Al_2O_3 layers reach best passivation properties in nominal or slightly O-rich stoichiometry ([O]/[Al] $\geq$ 1.5) [70, 105].

Table 2.1 Typical process settings in PECVD of silicon surface passivation layers achieving S_{eff} < 10 cm/s after annealing. The abbreviation TMA stands for trimethylaluminium $Al(CH_3)_3$

Material	Precursor gases	Process ambient	References
SiN_x:H	SiH_4 + NH_3	350–450 °C	[134–137]
SiO_2 (SiN_x)	SiH_4 + N_2O	250–350 °C	[138, 139]
Al_2O_3	TMA + CO_2 ($+H_2$)	200 °C	[133, 140]
	TMA + O_2/Ar	200–300 °C	[76, 141]
	TMA + N_2O	350 °C	[94, 142–144]

2.3.2 Atomic Layer Deposition

ALD processes for oxides are based on a sequence with two surface reactions (Fig. 2.11). These sequential gas-surface reactions are called 'half-reactions'. During the first half-reaction, the precursor gas is pulsed into the reactor chamber until the substrate surface is fully adsorbed by the precursor gas. Subsequently, the chamber is purged with an inert carrier gas (typically N_2 or Ar) to remove any unreacted precursor or by-products of the reaction. This is then followed by an oxidizing agent pulse, which reacts with the adsorbed precursor molecules to the oxide. Finally, the chamber is purged to remove the reactants. Subsequently, this process is cycled until the thickness target is reached. As the process is self-limited by the gas adsorption to the substrate, the growth can be controlled on a single layer level. The growth per cycle (GPC) values depends on reactant gases and process temperature. Typical values are 1 Å/cycle for Al_2O_3, SiO_2 and HfO_2 and 0.3 Å/cycle for TiO_2.

Because the surface reactions are performed sequentially, the two gas phase reactants are not in contact in the gas phase. This separation of the two reactions limits possible gas phase reactions that can form particles and produce granular films after deposition on the surface. As a result, ALD films grow extremely smooth and conformal. Because of the homogeneous coverage with reactants no surface sites are left behind during film growth and the films tend to be very continuous and pinhole-free [146]. These factors result in excellent surface passivation properties of ALD-grown layers.

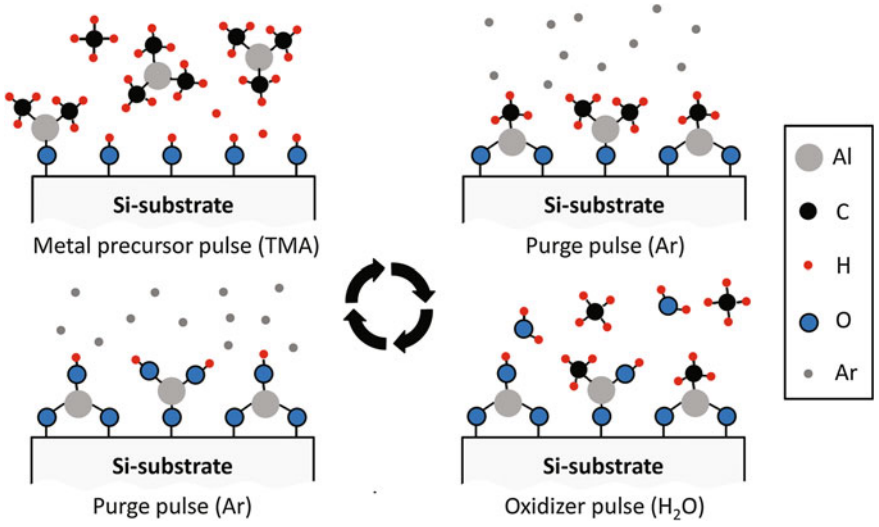

Fig. 2.11 Schematic drawing of the Al_2O_3 ALD process with TMA and H_2O precursors. The ALD cycle comprises of two half reactions with a sequence of metal precursor and oxidizing agent separated by purge pulses (according to [145])

The first investigations on ALD-grown Al_2O_3 passivation layers were published only one decade ago [40, 147]. Triggered by the excellent material properties of Al_2O_3, intensive research followed on new materials and processes. Today, excellent passivation performance has been demonstrated for numerous ALD-grown materials (Table 2.2). Interestingly enough, the most common passivation material, i.e. SiN_x:H, cannot be found in this list. The plasma enhanced ALD process of silicon nitride is developed for the application in microelectronic devices [148, 149]. However, reasonable surface passivation of this material has not been reported yet. One of the barriers is the stoichiometric nature of ALD-grown silicon nitride, i.e. Si_3N_4, whereas good passivation performance is achieved Si-rich films.

In the conventional temporal ALD the precursors are sequentially dosed into the reaction chamber and separated in time by purge pulses. ALD tools in research and microelectronic manufacturing are usually based on temporal processing. To meet the demand for high-throughput and low-cost equipment for solar cell manufacturing, spatial ALD concepts were introduced recently. In spatial ALD, the precursors are supplied continuously but the two reactions are spatially separated. The reactor contains two zones where the half-reactions take place. The ALD cycles are realized by moving the substrates between these two zones [159]. Spatial ALD systems are designed for industrial throughput above 1000 wafers/h. Several studies reveal the excellent passivation quality of spatially ALD-grown Al_2O_3 on wafers [150] and solar cells [160, 161].

Table 2.2 Typical process settings in ALD of silicon surface passivation layers achieving $S_{eff} < 10$ cm/s after annealing. The abbreviations BDEAS stands for bis(diethylamino)silan $H_2Si[N(C_2H_5)_2]_2$, TEMAHf for tetrakis(ethylmethylamino)hafnium $Hf[N(CH_3)C_2H_5]_4$ and TTIP for titanium tetraisopropoxide $Ti(C_{12}H_{28}O_4)$, respectively

Material	Precursor 1 (metal precursor)	Precursor 2 (oxidizing agent)	Process ambient	References
Al_2O_3	TMA	H_2O	100–300 °C	[6, 76, 105, 150, 151, 153]
		O_2 plasma	100–300 (500) °C	[6, 40, 76, 105, 119]
		O_3		[6, 105, 152]
SiO_2	BDEAS	O_2 plasma	150–200 °C	[79, 153]
HfO_2	TEMAHf	O_2 plasma	200 °C	[154]
		H_2O	150–200 °C	[109, 151 153]
	Trimethyl-hafnium	H_2O	300 °C	[72]
TiO_2	TTIP	H_2O	200–250 °C	[87, 151]
	$TiCl_4$	H_2O	100–200 °C	[155, 156]
Ta_2O_5 (SiN)	Tantalum-ethoxide	H_2O	250 °C	[157]
Ga_2O_3	Trimethyl-gallium	O_2 plasma	75 °C	[158]

2.3.3 Alternative Deposition Methods

Though PECVD and ALD tools dominate the market today, novel techniques emerge due to their potential to reduce production costs and to replace the pyrophoric TMA process gas. Atmospheric pressure chemical vapor deposition (APCVD) is very interesting for industrial high-throughput applications because of the elimination of vacuum and consequently reduced equipment costs. Additionally, Al_2O_3 deposition is possible with the non-pyrophoric triethyldialuminum tri-(sec-butoxide) precursor [162]. Black et al. reached excellent surface recombination velocities of below 3 cm/s with APCVD-grown Al_2O_3. Similar to films grown by PECVD or ALD, APCVD-grown layers also contain negative fixed charges in the order of 10^{12} cm^{-2} providing high field-effect passivation. Additionally, films capped with SiN_x:H feature very good thermal stability during fast firing [163, 164]. APCVD was also used to deposit TiO_2 for surface passivation and antireflection coating [165, 166].

Another promising deposition technology is sputtering. Sputtering is a mature technique widely used in electronics and thin-film industries and it is available for large-scale processing. Sputtering targets consist of non-toxic materials. However, surface passivation properties of sputtered layers lag behind the performance achieved with established methods. Most publications on sputtered passivation layers report carrier lifetimes in the range of 100 µs or even below. One of the obvious drawbacks of sputtering is that the process does not involve an obvious source of hydrogen. Contrary to metal-organic precursor gasses, metallic or ceramic sputtering targets are free of hydrogen. It was shown that reactive sputtering with additional H_2 gas supply significantly improved the passivation performance of SiN_x:H [167] and Al_2O_3 [168]. Zhang et al. demonstrated carrier lifetimes up to 5 ms with hydrogen-sputtered Al_2O_3 [168]. Despite of this excellent value, the role of hydrogen is still under discussion. This discussion is inspired by the fact that hydrogen was also detected in high concentrations in sputtered Al_2O_3 layers [169] potentially caused by remaining water vapor in the vacuum chamber. Additionally, it is shown that process parameters and film stoichiometry are at least as important and lifetimes in the millisecond range are feasible even without additional hydrogen supply [83, 170].

Though sputtered passivation layers have not yet reached the high quality of films grown by the established methods, the achieved level is already sufficient for the application in highly efficient PERC solar cells. Schmidt et al. demonstrated an cell efficiency above 20 % with sputtered rear side Al_2O_3 passivation [171].

2.3.4 Low-Thermal Budget Processing

For some solar cell concepts the thermal budget is restricted (Sect. 2.1.2). For example, concepts involving a-Si:H require process temperatures below 200 °C.

ALD-grown Al_2O_3 is a potential candidate for low-thermal budget passivation, as an excellent level of passivation is already achieved at low deposition temperatures (Sect. 2.2.3.1). However, films grown at low temperatures still require a thermal activation at about 400 °C. Considering hydrogenation of interface defects as a thermally activated process with associated activation energies (2.7) and (2.8), it appears difficult to by-pass this process at low temperatures. Lower temperatures might be compensated by longer annealing periods; however, long term annealing potentially also harms the temperature sensitive substrate.

The thermal budget of the annealing process could be reduced by optimized process parameters. Vandana et al. investigated reduced process times during annealing in N_2 atmosphere at 400 °C. The authors found carrier lifetimes above 1 ms already after 100 s of annealing. The passivation level increased with thickness and the best values were found for 100 nm thick Al_2O_3 layers [172]. Seguini et al. investigated Al_2O_3 annealing at 200 °C and found carrier lifetimes up to 1 ms when using layers, which were deposited at ALD process temperatures below 150 °C [173]. Due to enhanced incorporation of hydrogen during layer growth, low deposition temperatures increase the reaction rate during the hydrogenation process (Sect. 2.2.3.1). Therefore, the combination of low deposition and low annealing temperatures appears very promising [106, 107, 173]. However, the reduction of the thermal budget often results in a lower level of passivation. Electrical characterization reveals a reduced field-effect passivation and partly lower chemical passivation [172, 173] indicating that the passivation process is not fully completed.

Another approach to reduce the thermal budget is flash light annealing (FLA). This technique is known from various applications in microelectronics, e.g. doping activation [174], thermal treatment of high-*k* dielectrics [175] or flash-enhanced deposition techniques [176]. FLA employs a short light flash, typically in the millisecond range, to induce a short-term heating process [177]. During the flash, the uppermost region of the substrate is rapidly heated to high temperatures while the backside only experiences moderate heating [178]. Furthermore, the substrate acts as heat sink resulting in rapid cooling after the flash. A schematic drawing of the flash light setup and the surface temperature as a function of time are shown in Fig. 2.12.

Simon et al. applied the FLA technique to Al_2O_3 passivation layers [106]. Figure 2.13 shows the carrier lifetime as a function of flash iteration, annealing atmosphere and deposition process. The best result is achieved for Al_2O_3 grown by thermal ALD after FLA in H_2 atmosphere at 200 °C (Fig. 2.13a). In the as-grown state, the carrier lifetime is poor (3 µs) but it quickly increases to 455 µs after a single FLA cycle and reaches 5 ms after 100 cycles, which is comparable to values reached after reference annealing at 350 °C. FLA of samples grown by plasma enhanced ALD also results in a significant increase of carrier lifetime; however, the values hardly exceed 1 ms and clearly remain below the result of the standard anneal (Fig. 2.13b). Processing in Ar instead of H_2 atmosphere also results in lower carrier lifetimes.

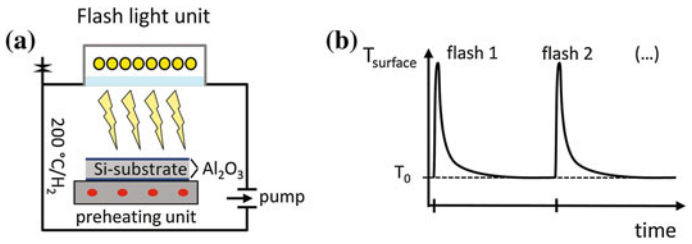

Fig. 2.12 Schematic drawing of a FLA setup (**a**) and surface temperature ($T_{surface}$) versus process time (**b**). The flash light induces a short-term temperature peak at the surface. After the flash, the surface rapidly cools down to the substrate temperature (T_0)

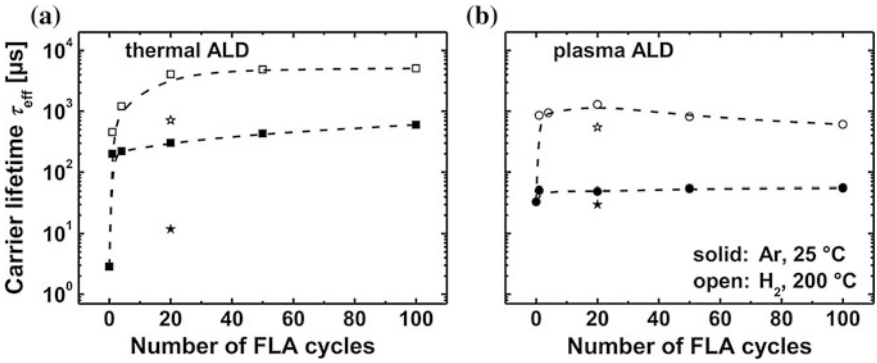

Fig. 2.13 Carrier lifetime as a function of FLA cycle numbers. The Al_2O_3 layers are deposited by thermal (**a**) and plasma enhanced (**b**) ALD. Reference samples with single-side FLA are plotted as *star symbols*. Reprinted with permission from Phys. Status Solidi RRL **9**, 631–635. Copyright 2015, John Wiley and Sons [106]

The different results after FLA are related to the effectiveness of interface hydrogenation at low process temperatures. In Al_2O_3 grown by thermal ALD, a high hydrogen incorporation facilitates the hydrogenation of the interface [105]. Contrary, plasma ALD-grown Al_2O_3 suffers from a higher interface state density in the as-grown state due to increased surface damage by exposure to oxygen radicals. Therefore, the thermal process provides a more suitable microstructure with a higher reaction rate for the hydrogenation process. Additionally to the influence of the microstructure, the surface passivation process is supported by H_2 atmosphere and enhanced temperature (200 °C). When further increasing the annealing temperature, the microstructure influence reduces due to the higher thermal budget involved. After reference annealing at 350 °C, samples grown by plasma and thermal ALD reach comparable carrier lifetimes of about 5 ms.

Flash light annealing is surface selective. When applying single-side FLA (Fig. 2.13, star symbols), the carrier lifetimes remain on a low level as single-side passivation could not improve the carrier lifetime by more than the factor of two,

when lifetime is limited by surface recombination [46]. The small increase of carrier lifetime corresponds to the pure effect of process ambient, i.e. substrate temperature and process atmosphere. To activate the passivation layers on both wafer sides, FLA has to be applied on the front and rear side of the substrate. This surface selectivity of FLA provides high thermal activation on one wafer side, whereas the temperature budget remains low at other side. Therefore, FLA opens the possibility to combine dielectric surface passivation with low-thermal budget solar cell concepts.

2.4 Dielectric Multi-oxide Nanolaminates

The introduction of multi-oxide nanolaminates opens the possibility to tailor material properties and functionalities for novel passivation layers. Multi-oxide nanolaminates are used to realize symmetrical (Sect. 2.4.1) and conductive (Sect. 2.4.2) passivation layers. These nanolaminates are grown by ALD, due to the accurate thickness control and the possibility to combine many different materials in one process step.

2.4.1 Zero-Fixed-Charge Passivation Layers

Dielectric multi-oxide nanolaminates make it possible to control the fixed charges and even reduce their density to zero. Zero-fixed-charge nanolaminates are realized in Al_2O_3 passivation layers with a very thin interface layer of SiO_2 [55, 127], Al-doped SiO_2 (Al:SiO_2) [73] or HfO_2 [153] on moderately doped silicon. Additionally, the concept was demonstrated with SiO_2/Al_2O_3 stacks on p^+ and n^+-doped Si substrates [27]. Figure 2.14 displays the density of fixed charges in these stacks as a function of interface layer thickness, which is plotted as ALD cycle number. At zero ALD cycle, i.e. in pure Al_2O_3, a high density of negative fixed charges ($3–4 \times 10^{12}$ cm^{-2}) is found. By increasing the ALD cycle number, the negative fixed charges gradually disappear. The required interface layer thickness for charge annihilation is about 10 cycles for SiO_2 and 5 cycles for HfO_2. Considering a steady state growth rate of about 1.2 Å/cycle for both materials, the interface layer thickness corresponds to a few monolayers only. The Al:SiO_2 interface layer was introduced because of the lower passivation level of ALD-grown SiO_2 compared to the level reached with Al_2O_3 [73, 79]. The doping was realized by 1:1 ALD super-cycles of SiO_2 and Al_2O_3. Zero fixed charge density is achieved after about five super-cycles (steady state growth rate: $\sim$2.5 Å/super-cycle).

When the interface layer thickness is further increased, the properties of this layer determine the charge formation. For HfO_2, the density remains zero as HfO_2 is almost free of charges under the applied ALD process settings [151, 153]. For SiO_2, the charge polarity turns from negative to positive above 10 ALD cycles and the

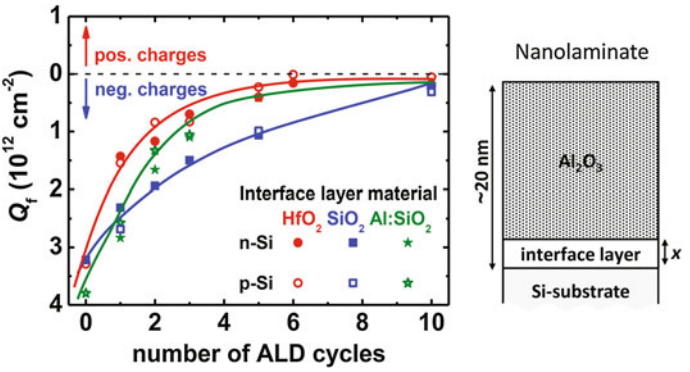

Fig. 2.14 Fixed charge density as a function of the interface layer material and thickness plotted as ALD (super-)cycle number. The charge density decreases with increasing interface thickness. The lines are guides to the eye. The nanolaminate layout is shown at the *right side*. Reprinted with permission from IEEE 42th Photovoltaic Specialists Conference (PVSC), 1–6. Copyright 2015, IEEE [73]

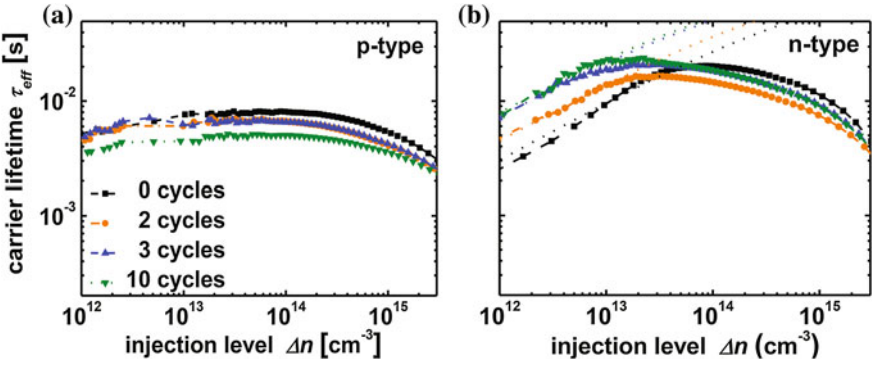

Fig. 2.15 QSSPC measurements of carrier lifetime as a function of the injection level for HfO_2/Al_2O_3 nanolaminates on *p*-type (**a**) and *n*-type (**b**) Si. The thickness of the HfO_2 interface layer was varied. *Dotted lines* are calculated using (2.4) and (2.6). Reprinted from Sol. Energy Mater. Sol. Cells **131**, 72–76, Copyright (2014), with permission from Elsevier [153]

density increases to 1–2 × 10^{12} cm^{-2} for thick SiO_2 layers [109, 179]. The substrate doping has no influence on the fixed charge formation, i.e. the same charge density is formed on *p*- and *n*-type Si.

The influence of fixed charge density on the carrier lifetime is different on *p*- and *n*-type Si substrates (Fig. 2.15). Both types of substrates are passivated with a nanolaminate comprising 20 nm Al_2O_3 and an HfO_2 interface layer with different ALD cycle numbers. On *p*-type Si, the carrier lifetime reaches values up to 8.0 ms and the values are almost independent on the interface layer thickness in the low

thickness regime (Fig. 2.15a). Only at 10 cycles of HfO_2, the carrier lifetime slightly decreases (5.5 ms). The measured carrier lifetimes are also independent of the injection level for $\Delta n < 1 \times 10^{15}$ cm^{-3}.

On *n*-type Si, the observation is different because the negative charges in Al_2O_3 invoke a surface inversion layer resulting in near surface recombination (Sect. 2.2.2). For low injection levels ($\Delta n < 5 \times 10^{13}$ cm^{-3}), the carrier lifetime strongly decreases (Fig. 2.15b). However, this degradation could be inhibited by introducing the HfO_2 interface. At an injection level of 5×10^{12} cm^{-3}, the carrier lifetime increases from 6.0 ms for pure Al_2O_3 to 9.5 ms and 15.0 ms for Al_2O_3 with two and three ALD cycles of HfO_2 interface layer, respectively. Additional ALD cycles do not result in higher carrier lifetimes and the effect saturated. At high injection level ($\Delta n = 1 \times 10^{14}$ cm^{-3}), all samples show comparable values of about 10.0 ms, independent of their HfO_2 interface layer thickness.

The reduction of fixed charges results in symmetrical passivation as the near surface recombination is suppressed in *p*- and *n*-type Si substrates. However, because of the absence of field-effect passivation the chemical passivation becomes more critical. Symmetrical passivation layers only rely on chemical passivation, i.e. a very low density of interface defects. The results of this section show that this high level of chemical passivation could be realized with multi-oxide nanolaminates.

An "inert" spacer model was proposed for interpretation of the fixed charge modification in Al_2O_3 [109]. Fixed charges in Al_2O_3 are linked to structural defects and the stoichiometry deviation in the initial growth regime of Al_2O_3 (Sect. 2.2.3.3). An additional interface layer interferes with this initial growth process as it interrupts the contact to the crystalline silicon substrate. The domination of tetrahedral coordination of Al in $AlO_{4/2}^-$ units requires a physical contact to the tetrahedrally oriented Si/SiO_x interface [114, 115]. This contact is interrupted by an interface layer. In HfO_2, the Hf-atom is 8-fold coordinated [180] and this different structure efficiently suppresses the growth of tetrahedrally coordinated Al in Al_2O_3. The SiO_2 spacer is less effective than the HfO_2 layer in a sense that the required layer thickness for charge annihilation is twice as large. ALD-grown SiO_2 does not suppress the tetrahedral coordination of the SiO_x/Si interface as efficiently due to its similar chemical structure.

2.4.2 *Carrier Selective Contacts*

2.4.2.1 Concepts of Carrier Selective Contacts

In general, carrier selective contacts consist of a medium with different conductivities for majority and minority carriers [28]. The medium is transparent to majority carriers, which are passed through to the electrical contact. However,

minority carrier transport is blocked and no recombination occurs within this medium or at its surfaces. Such carrier selective contacts have been realized in

- a-Si:H/c-Si heterocontacts (Fig. 2.16a), which are applied in silicon heterojunction solar cells [22]. In this concept, the carrier selectivity is implied by the band offsets between a-Si:H and c-Si. The majority carrier transport through the heterocontact is constituted by thermionic emission or tunneling in the presence of band bending. Owing to the excellent carrier selectivity, this concept reaches highest open circuit voltages up to 750 mV and efficiencies up to 24.7 % for both-side contacted solar cells [18].
- tunneling contacts (Fig. 2.16b), which comprise a high band gap tunneling oxide and a transport matrix. SiO_2 [181–183] and Al_2O_3 [184, 185] are common tunneling oxide materials due to their high band gap and low defect density at the interface to silicon. For the transport matrix, microcrystalline or amorphous silicon are used. Alternatively, transparent conductive oxides are investigated such as ITO or ZnO for contacts on *n*-type Si [184, 186] and WO_x or MoO_x for contacts on *p*-type Si [186]. The electrical conductivity is optimized by tailoring the tunneling probability, which is mainly determined by oxide thickness and transport matrix parameters including work function and band gap energy [187, 188]. Though the development of tunneling contacts gained momentum only a few years ago, several groups already integrated this concept into solar cells and demonstrated very high efficiencies [185, 189] of up to 24.4 % [190].

Carrier selective contacts can also be realized with dielectric multi-oxide nanolaminates (Fig. 2.16c). Promising candidates are Al_2O_3–TiO_2 nanolaminates, which combine the excellent surface passivation properties of Al_2O_3 with the higher conductivity of TiO_2 [73, 87]. Al_2O_3–TiO_2 passivation laminates are shown to feature superior properties compared to pure Al_2O_3 layers in terms of surface recombination [151] and optical properties [191, 192]. These nanolaminates have

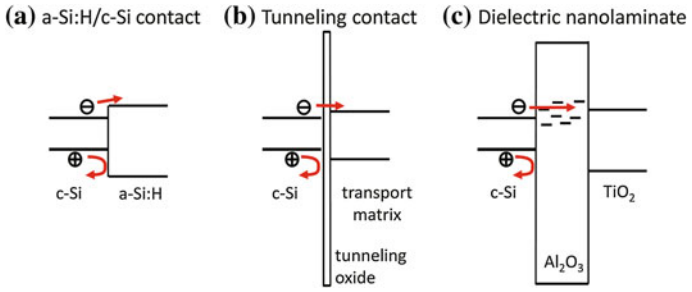

Fig. 2.16 Different concepts for carrier selective contacts on *n*-type silicon. The carrier selectivity is achieved by the band offsets at the a-Si:H/c-Si heterocontact (**a**), the tunneling probability at the tunneling contact (**b**) and the specific electrical transport properties at the dielectric nanolaminate (**c**)

also been intensively investigated for the application as gate dielectrics in microelectronic devices. The incorporation of TiO_2 is found to increase the *k*-value of the gate stack; however, it also strongly enhances the leakage current, which degrades the device performance. Both parameters can be controlled by the stacking sequence and sublayer thicknesses in the Al_2O_3–TiO_2 nanolaminates [193, 194]. For carrier selective contacts, the Al_2O_3–TiO_2 stack layout is optimized for high conductivity and high level of surface passivation. The main advantage of dielectric Al_2O_3–TiO_2 nanolaminates over other concepts is the strong synergy with today's PERC technology:

- Dielectric layers act as very effective optical reflectors at the rear side of the solar cell due to their relatively low refractive index of below 2 (Sect. 2.5.1). Carrier selective contacts with Si-based transport matrices often feature attenuated rear side reflection and require additional measures for light management to achieve the same level of absorption than realized in PERC solar cells.
- Dielectric materials provide a reasonable level of temperature stability, which is required during the fast firing step in the PERC process sequence. Carrier selective contact concepts partly have a restricted thermal budget, especially when a-Si:H is used as transport matrix. An integration of these concepts into the PERC solar cell would require a thermal budget reduction with major consequences, especially for the metallization strategy.
- Dielectric nanolaminates can be deposited by ALD and in principle also by PECVD. As the required equipment is already implemented in today's PERC manufacturing, the conversion from a point contact to a full area carrier selective contact scheme could be realized with low equipment invest.

2.4.2.2 Al_2O_3–TiO_2 Carrier Selective Contacts

The electrical properties of Al_2O_3–TiO_2 nanolaminates are essentially determined by the stack layout. Figure 2.17 shows the results of double and multilayer stacks on *p*-type Si substrates. Both stacks comprise an Al_2O_3 interface layer due to its better surface passivation. TiO_2 serves as a capping layer in the double layer stack. Al_2O_3–TiO_2 multilayers consist of alternating Al_2O_3 and TiO_2 sublayers of equal thickness and an adjusted number of iterations in order to maintain a total nominal thickness of 20 nm. The measured carrier lifetime as a function of the Al_2O_3 interface layer thickness x shows that pure TiO_2 passivation (x = 0 nm) results in poor carrier lifetime (τ_{eff} < 100 µs). This result is not surprising as the passivation level of TiO_2 is known to be inferior to the one of Al_2O_3 [122, 154, 155]. When increasing the interface layer thickness, the carrier lifetime continuously improves. The highest value of 5 ms is measured with pure Al_2O_3 (x = 20 nm) passivation. This correlation is observed for double and multilayer stacks, i.e. the passivation performance is independent of the stack above the first TiO_2 (sub)layer. Essentially, the lifetime is determined by the distance of the first TiO_2 layer to the silicon surface [151].

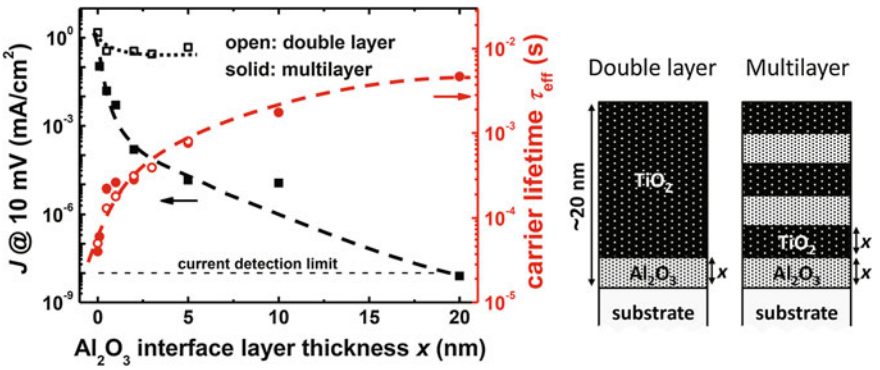

Fig. 2.17 Current density (at 10 mV) and carrier lifetime of different double layers (*open dots*) and multilayers (*solid dots*) as a function of the Al_2O_3 interface thickness x. Substrate material is p-type Si. The nanolaminate layout is shown at the *right side*. Reprinted with permission from IEEE 42th Photovoltaic Specialists Conference (PVSC), 1–6, Copyright 2015, IEEE [73]

Figure 2.17 also shows the measured current densities J at 10 mV. This voltage drop is chosen as an acceptable voltage loss at the contact. The electrical data are plotted as current densities rather than contact resistance because of the non-ohmic behavior of a part of the investigated stacks. The conductivity of pure Al_2O_3 is very low and the current density is below the measurement limit (10^{-8} mA/cm^2). In pure TiO_2, the current density is at least eight orders of magnitude higher. The influence of the Al_2O_3 interface layer thickness is different for both stack types. For multilayer stacks, the current density drastically drops with increasing thickness. In the double layer stack, the reduction is comparatively low. A 5 nm Al_2O_3 interface layer still results in a current density of about 0.5 mA/cm^2. This value is about four orders of magnitude higher than the current density of a multilayer stack with the same sublayer thickness.

In double layers, the current density is almost independent of the Al_2O_3 interface layer thickness, suggesting the electrical transport is not constituted by electron tunneling. The electrical properties of the nanolaminates are suggested to be determined by a TiO_2 phase transformation from amorphous to anatase and an interaction of TiO_2 and Al_2O_3. The phase transformation occurs when a critical layer thickness of about 10 nm is exceeded in ALD-grown TiO_2 layers [195, 196]. As the different conductivities of both stack types correlate with the appearance of anatase TiO_2 [87], the crystallization of the TiO_2 capping layer is suggested to weaken the insulating properties of Al_2O_3 resulting in good conductivity even through 5 nm thick layers. Potential transport processes through the Al_2O_3 interface layer are hopping through impurities levels (as shown in Fig. 2.16c) or pin-hole transport [197].

The Al_2O_3–TiO_2 double layer with x = 5 nm features the best balance of electrical transport and surface passivation with 0.5 mA/cm^2 current density (at 10 mV) and 15 cm/s surface recombination velocity. Compared to the requirements of a highly efficient solar cell [7], this nanolaminate features sufficient passivation performance. However, the current density is still about two orders of magnitude

below target (40 mA/cm^2), although the Al_2O_3–TiO_2 nanolaminates strongly enhanced the conductivity compared to standard Al_2O_3 passivation layers. In conclusion, the electrical properties of Al_2O_3–TiO_2 nanolaminates can be controlled by stack layout and sublayer thicknesses within a wide range. With further improvements of conductivity, dielectric Al_2O_3–TiO_2 nanolaminates could provide powerful solutions for future carrier selective contacts.

2.5 Dielectric Materials and Light Management

Dielectric passivation layers are also part of the solar cell light management. Therefore, the optical properties of these layers have to be optimized. In the state-of-the-art PERC solar cell, dielectric nanomaterials control the surface reflections at the front and rear side (Fig. 2.18a). Additionally, dielectric materials are applied in novel light trapping and spectral conversion concepts.

2.5.1 Dielectric Layers for Surface Reflection Control

A planar Si surface appears like a mirror plane. Owing to the relatively high refractive index of Si (n_{Si} = 3.8 at 633 nm), the surface reflection of polished silicon is about 34 % making reflection control and the application of anti-reflection coating (ARC) essential.

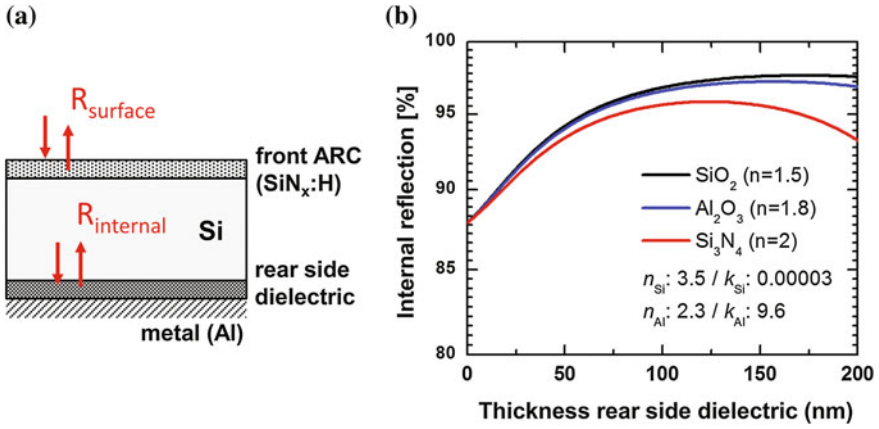

Fig. 2.18 Optical reflections at the front and rear surfaces of a PERC solar cell (**a**) and simulation of the internal reflection (λ: 1100 nm, angle of incident: 0°) as a function of thickness and material of the rear side dielectric layer (**b**). Optical parameters used for simulation are stated in the plot

For a single-layer, non-absorbing ARC, the reflection at perpendicular angle of incident becomes zero when the ARC thickness is optimized and the refractive indices of the materials are matched [198]:

$$d_{\mathrm{ARC}} = \frac{\lambda}{4n_{\mathrm{ARC}}} \text{ and } n_{\mathrm{ARC}} = \sqrt{n_{\mathrm{Si}} n_{\mathrm{ambient}}} \tag{2.10}$$

with d_{ARC} the ARC thickness and n the refractive indices of the materials. A system optimized for the peak intensity of sun light (633 nm) requires an ARC with refractive index of $n_{\mathrm{ARC}} = 1.95$ when the ambient is air ($n_{\mathrm{ambient}} = 1$, $n_{\mathrm{Si}} = 3.8$). The resulting ARC thickness is 80 nm. In solar cell manufacturing, minimum reflection losses are targeted within the module stack, where the ambient is defined by the packaging material consisting of lamination foil (e.g. EVA) and glass cover with a refractive index of about 1.5. Considering the packing material in (2.10), the optimum refractive index of the ARC shifts to a higher value. Consequently, the ARC material properties have to be optimized for either encapsulated or non-encapsulated solar cells. The calculation of optical reflection becomes more complex when considering the full relevant wavelength range, different angles of incident, the spectral response of the solar cell and the absorption coefficient of the ARC layer. A thorough optimization of the antireflection strategy usually employs numerical simulation [136, 199, 200].

The standard front side ARC material is SiN_x:H and its main advantage is the possibility to continuously tune the refractive index within a wide range. In the PECVD process, the stoichiometry of the film is controlled by the process gas ratio, which allows to continuously increase the refractive index from 1.9 (a-Si_3N_4:H) to 3.3 (a-Si:H) [201]. The optimum SiN_x:H ARC layers are thus Si-rich with [Si]/[N] > 3/4. The tunability by a gradual replacement of reactant gases can also be used to create graded index ARC layers with minimized surface reflection [202].

At the rear side of the solar cell, high internal reflection is targeted for the near band gap spectral range (1000–1100 nm), which is weakly absorbed in Si. As band-to-band absorption increases with photon energy, the shorter wavelength part of the spectrum is mainly absorbed within the Si wafer and hardly reaches the rear side of the wafer. Figure 2.18b shows the effect of a rear side dielectric layer on the internal reflection at a wavelength of 1100 nm. The reflection is about 88 %, when the Si rear side is terminated by an Al electrode, which is the contact scheme in a back surface field (BSF) solar cell. This relatively low reflection seems surprising since metals are known to be highly reflective in the IR spectral range. However, at the Si–Al interface the high refractive index of Si leads to considerably suppressed reflection compared to the reflection at the air-Al interface [8]. When Si and Al are separated by a low refractive index dielectric layer, the optical contrast of the interfaces is enhanced and the internal reflection significantly increases. The simulated internal reflection is a function of the stack parameters with highest values above 97 %, which are reached for dielectric materials with low refractive index and a matched layer thickness in the range of 100 and 200 nm.

Based on these simple optical simulations, the optimum dielectric layer thickness is larger at the rear side of the solar cell. Therefore, the SiN_x:H capping layer is not only required to improve the temperature stability of the rear side passivation layer but also to enhance the internal reflection. Beside of the reduction of surface recombination, the improved rear side light management is one of the main advantages of the PERC solar cell concept [8, 9]. This improvement can be measured as reduced reflection at the solar cell surface in the wavelength range between 1000 and 1200 nm [203, 204]. Reduced reflection consequently leads to higher quantum efficiencies of the PERC solar cells compared to cells with direct Si–Al contact (BSF solar cells) [9, 205].

2.5.2 *Concepts for Light Trapping*

Reflection control alone has only limited potential for absorption enhancement, especially when substrates become thinner and when high quantum efficiencies are targeted for the near band gap spectrum. Figure 2.19a shows a planar wafer with an incident light ray at perpendicular angle of incident. Considering a perfect reflection control on both surfaces, the light path through the system is twice the substrate thickness. After passing the substrate, the non-absorbed photons escape through the front surface. Therefore, light scattering features are introduced to enhance the light path and to trap the light within the absorber layer.

The effect of light scattering can be theoretically described by ideal Lambertian surfaces, which create a diffuse light spectrum with a statistical phase-space intensity distribution. When sunlight passes a Lambertian scatterer, the light path is enhanced and the light is then totally reflected within the surfaces until it escapes. As a consequence, the internal light intensity manifold exceeds the intensity of incident light in the sustrate. Based on statistical ray optics, Yablonovitch calculated this intensity enhancement factor as $2n^2$ with n the refractive index of the substrate under the assumption that the rear side is perfectly reflecting [206]. The resulting optical absorption enhancement is $4n^2$. A Lambertian scattering surface could thus enhance the absorption up to a factor of 50 in Si.

In crystalline silicon based solar cells, the surface is structured with randomized pyramids in a typical length scale of 10 µm (Fig. 2.19b) [207]. The texturing

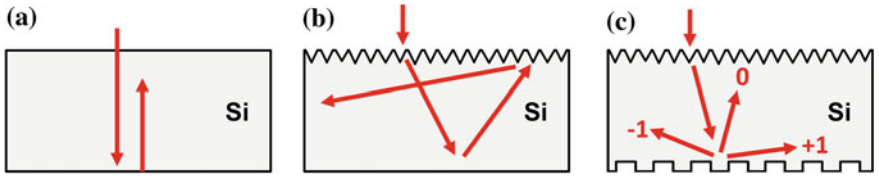

Fig. 2.19 Light path enhancement strategies in solar cells employing planar surfaces (**a**) a textured front surface (**b**) and an additional periodic structures at the rear surface (**c**)

process is based on anisotropic (i.e. orientation dependent) wet etching with an alkali (KOH or NaOH) etch solution. Alkaline etchants remove the (100) plane of Si much faster than the (111) plane and the result is a 3D pyramidal structure [208]. For crystalline wafers it was shown that randomized pyramids with optimized geometry get close to the $4n^2$ absorption limit of Yablonovitch [207, 209]. For multi-crystalline wafers with random crystal orientations this technique is much less effective since only grains with close to (100) orientation are well textured while grains with (111) orientation still remain highly reflective. Multi-crystalline wafers are usually textured with acid solutions resulting in a rough scattering surface. The resulting absorption enhancement is below the enhancement achieved on textured Si surfaces [210, 211].

Further enhancement of light trapping is possible with advanced photonic features, which exploit the wave nature of the light (Fig. 2.19c) [212, 213]. For periodic patterns the reflection is described by the diffraction equation [198]:

$$\sin(\theta_m) - \sin(\theta_i) = \frac{m\lambda}{nP} \tag{2.11}$$

with the wavelength λ, the order m, the grating period P, the refractive index n and the angles of incident Θ_i and diffraction Θ_m defined w.r.t. the surface nominal. Periodic gratings provide very powerful absorption enhancement when the diffracted light intensity is concentrated at high angles and the light transverse a long path through the solar cell before it escapes through a surface. Using (2.11), high first order (m = ±1) diffraction angles are reached when $\lambda \leq nP$. Thus, light absorption enhancement of the near band gap spectrum requires scattering features on micrometer scale. Periodic structures could significantly increase light trapping even beyond the limit of Lambertian light scattering [214–216].

Several techniques are applied to fabricate photonic nanostructures including nanoimprint [217, 218], laser interference [213], e-beam [219] and holographic [220] lithography. As an example, one concept generating the periodic optical contrast with dielectric materials is shown in Fig. 2.20. Eisenlohr et al. deposited a hexagonally ordered monodisperse SiO_2 sphere grating by spin coating on the rear side of a solar cell (Fig. 2.20a). These low refractive index spheres were embedded in a high refractive index matrix of polycrystalline Si deposited by APCVD [221, 222]. These spheres significantly improved the light absorption in the IR region (Fig. 2.20b) resulting in a higher short circuit current. Planar solar cells with back side scattering spheres reach an efficiency of 22.1 %.

2.5.3 *Spectral Conversion of Light*

In a single junction solar cell the sub-band gap light spectrum is not utilized. With photon up-conversion low-energy photons are converted into ‘useful’ photons ($hv > E_\mathrm{g}$) having sufficient energy to be absorbed in Si. The up-conversion process

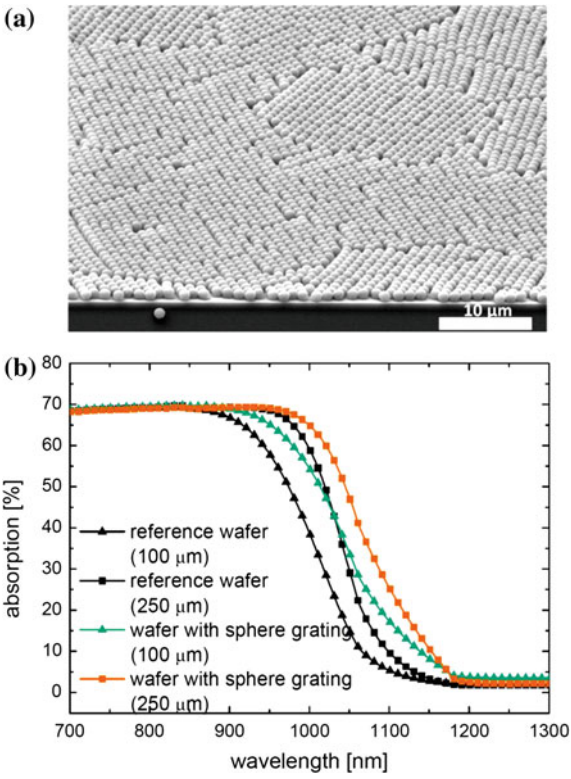

Fig. 2.20 SEM picture of a dielectric rear side grating consisting of SiO_2 spheres after spin coating (**a**) and absorption spectra measured with and without sphere grating on 100 and 250 µm thick wafers. The improved light trapping significantly increases the light absorption in the IR region. Reprinted with permission from Optics Express **22**, A111–A119, Copyright 2014, Optical Society of America [222]

is possible in trivalent lanthanide ions with metastable and long-lived intermediate levels. These ladder-like levels act as intermediate levels for the sequential excitation. The principal transitions in common lanthanide are summarized in [223]. Suitable ions with energy levels in the Si sub-band gap energy range are Er^{3+}, Tm^{3+} and Ho^{3+}, whereas the Er^{3+} ion is the most investigated material in combination with Si [29, 224, 225]. The energy levels of Er^{3+} are depicted in Fig. 2.21. Er^{3+} has a rather narrow absorption band at 1.56 µm (0.8 eV), which is capable of absorbing sub-band gap photons for up-conversion. To broaden the utilized spectral range, Lahoz et al. combined Er^{3+} and Ho^{3+} up-conversion layers. Ho^{3+} ions have an absorption band at 1.17 µm (1.06 eV), where the solar irradiation intensity is about twice as high as the intensity at the absorption band of Er^{3+} [226].

These lanthanide-based conversion ions are hosted in a matrix, which requires a low lattice mismatch to the dopant ions and low phonon energies. The low phonon energy suppresses non-radiative transitions between closely spaced energy levels due to multiphonon relaxation. The most commonly used matrix material for Er^{3+} is β-$NaYF_4$, however, several other materials such as β-BaY_2F_8 or fluoride glasses are investigated as well [29, 223].

Several mechanisms of up-conversion have been identified. The simplest up-conversion mechanism involves sequential photon absorption from the ground

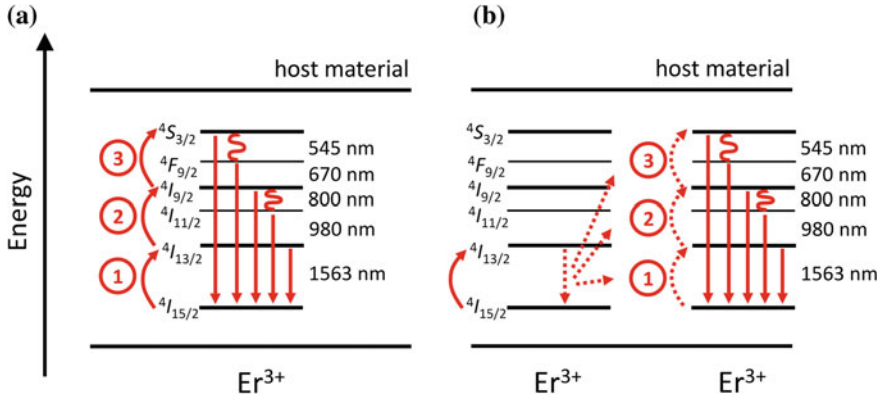

Fig. 2.21 Principal up-conversion mechanisms in Er^{3+} ions. The excited state absorption (**a**) involves a single ion. The energy transfer up-conversion (**b**) is based on the non-radiative energy exchange between two neighboring ions. Absorption/emission and energy transfer are indicated by *solid* and *dotted lines*, respectively. The sequential absorption steps are denoted by numbers. Energy levels are taken from [225, 229]

state to elevated excited states. This excited state absorption (ESA) process transfers a single ion to a higher energy level as illustrated in Fig. 2.21a. In the energy transfer up-conversion (ETU) two neighboring ions are involved. After both ions are excited into a meta-stable state, the ions then non-radiatively exchange energy. The activator ion is excited to a higher energy level and the sensitizer ion relaxes to the ground state (Fig. 2.21b). At high excitation powers also the photon avalanche mechanism results in up-conversion [223, 224]. After a two-step or multiple-step absorption process, the excited ion can emit one photon exceeding the Si band gap energy. This photon generates electron-hole pairs in the solar cell and thus increases the spectral response at an energy level corresponding to the absorption band of the converter material.

Up-conversion is a non-linear process. When the process involves two or more photons for up-converted emission, theory predicts that the occupation of the uppermost excited state correlates to P^n, where P is the power density and n the number of photons involved. This non-linearity results in an external quantum efficiency (EQE) proportional to $P^{(n-1)}$, i.e. the EQE values linearly increases with illumination intensity for a two-photon absorption process. In experiments the exponent n was found to be close to the theoretical value of two at low irradiance. At higher power densities the exponent decreases as other processes, like non-radiative recombination, occur [225, 227, 228]. As a consequence of the power dependency of up-conversion, reasonable up-conversion efficiencies are only reached for high illumination intensities, which are typically only reached in concentrated sun light.

Up-conversion layers can be easily integrated in bifacial solar cells with a transparent rear side [228, 230]. The up-conversion layer is attached at the rear side of the solar cell and covered by an additional back reflector to reflect the anisotropic light emission back into the Si substrate. In principle, the up-conversion layer could

also be integrated at the front side. However, this configuration is less attractive due to parasitic absorption of photons exceeding the band gap energy and due to the fact that half of the up-converted anisotropic emission is directed away from the solar cell. Figure 2.22a depicts a bifacial solar cell with an Er-doped $NaYF_4$ up-conversion layer. This conversion stack reaches an enhanced quantum efficiency yield of up to 3.4 % at the absorption band of Er^{3+} under an illumination of 1000 suns (Fig. 2.22b) [227]. In this early work, up-conversion hardly enhanced solar cell efficiency at lower illumination intensities. More recent studies demonstrate photocurrent gains of 0.55 % at 94 suns [230] and 3.89 mA/cm^2 at 50 suns, which corresponds to about 0.2 % enhancement [231]. These photocurrent gains prove a significant progress during the last years; however, the low conversion efficiency is still an obstacle for commercialization of up-converter solar cells.

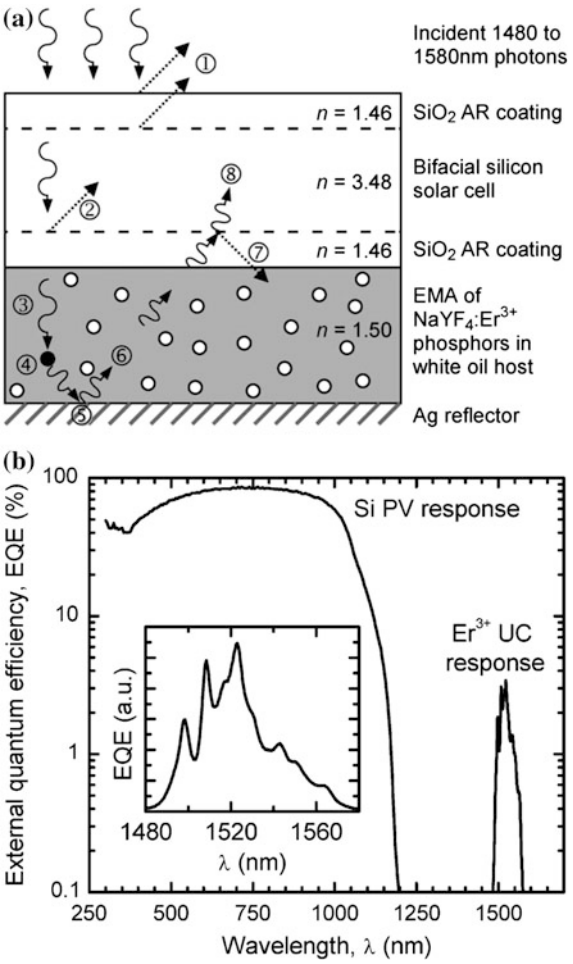

Fig. 2.22 Solar cell comprising a $NaYF_4:Er^{3+}$ up-conversion layer (**a**) and measured spectral quantum efficiency (**b**). The up-conversion process results in an increased photo-response centered at 1540 nm. Reprinted with permission from IEEE Transactions on Electron Devices **54**, 2679–2684, Copyright (2007), IEEE [227]

In most concepts, the up-conversion layer is attached to a functional solar cell. Alternatively, up-conversion layers could also be used for surface passivation and integrated into the solar cell concept, provided that the electrical quality of the host matrix is sufficient. Lanthanide oxides used for up-conversion can be deposited by ALD within a temperature range of 200–400 °C [232], which coincides with the temperature window of common passivation materials (Table 2.2). Dingemans et al. realized Er-doped Al_2O_3 layers and found up-conversion under 1480 nm wavelength illumination [233]. Al_2O_3 is found to be a suitable host matrix for Er^{3+} on condition that a post-deposition annealing above 900 °C is applied. During annealing, OH residuals are removed, which cause quenching of the Er^{3+} luminescence [234]. However, the high thermal budget required for optical activation of the Er^{3+} ions also degrades the passivation quality of Al_2O_3. Solar cells based on passivating conversion layers (Fig. 2.1f) have not been experimentally realized yet.

Down-conversion transfers a high energy photon ($>2E_g$) into two photons of lower energy [29, 235, 236]. Down-conversion layers have to be integrated at the front side of the solar cell, where high energy photons are not already absorbed within the Si substrate. This is a fundamental restriction for down-conversion, since down-converted photons are isotropically emitted and partly directed away from the solar cell. This escape loss strongly reduces the conversion efficiency. Therefore, research activity mainly focuses on up-conversion, though the theoretical potential of up- and down-conversion is similar.

2.6 Conclusions and Outlook

Dielectric nanomaterials are an essential element in today's silicon PERC solar cells. SiO_2, SiN_x:H and Al_2O_3 nanolayers were introduced due to their excellent properties for surface passivation and light management. The excellent surface passivation is achieved by chemical and field-effect passivation. The chemical passivation reduces the density of silicon surface states, which could act as recombination centers for photo-generated charge carriers. The field-effect passivation results from a high density of intrinsic fixed charges, which are located at structural defect sites at the interface of the dielectric to silicon. These fixed charges produce an electric field, which causes a strong asymmetry of the electron and hole concentrations at the surface and thus reduces charge carrier recombination.

The front side SiN_x:H passivation layer also serves as optical ARC. As the refractive index of PECVD-grown SiN_x:H can be continuously tuned within a wide range, the optical properties of the material can be optimized for lowest reflection losses at the front surface. Additionally, the dielectric passivation stack enhances the internal light reflection at the rear side of the PERC solar cell resulting in a significant improvement of the quantum efficiency in the IR spectral range.

However, novel solar cell concepts with higher efficiencies and lower production costs emerge and these concepts require further development of materials and processes. Flash light annealing appears as a promising solution to reduce the temperature

of the passivation process below 200 °C. A low-thermal budget process enables the combination of dielectric materials with low-temperature concepts, such as a-Si:H/c-Si heterojunction solar cells. Novel functionalities can be realized in multi-oxide nanolaminates employing materials, such as HfO_2 and TiO_2, which are not common in solar cell manufacturing today. Al_2O_3 nanolaminates with SiO_2 or HfO_2 interface layers provide symmetrical passivation with similar performance on both *n*- and *p*-type Si substrates. Al_2O_3–TiO_2 nanolaminates enhance the electrical conductivity of the passivation layer by several orders of magnitude without significantly deteriorating the passivation performance. These nanolaminates are very promising candidates for future carrier selective contact materials due to the strong synergy with today's PERC technology. Dielectric materials could also support future light management concepts as photonic scattering material or as host material for up-conversion layers.

Dielectric nanomaterials have been extensively studied for the application as high-*k* materials in microelectronic devices and this resulted in a profound understanding of material properties and mature deposition and characterization methods. This great knowledge base and the strong synergy between photovoltaics and microelectronics facilitated the integration of dielectric nanomaterials into Si solar cells in the past. However, this synergy is by far not exploited yet. Target of future R&D effort should be to further exploit this synergy and to realize novel functionalities for the next generation of highly efficient solar cells.

References

1. A.G. Aberle, Surface passivation of crystalline silicon solar cells: a review. Prog. Photovolt. Res. Appl. **8**, 473–487 (2000)
2. A.W. Blakers, M.A. Green, 20 % Efficiency silicon solar cells. Appl. Phys. Lett. **48**, 215 (1986)
3. J. Zhao, A. Wang, M.A. Green, 24.5 % efficiency silicon PERT cells on MCZ substrates and 24.7 % efficiency PERL cells on FZ substrates. Prog. Photovolt. Res. Appl. **7**, 471–474 (1999)
4. A.G. Aberle, R. Hezel, Progress in low-temperature surface passivation of silicon solar cells using remote-plasma silicon nitride. Prog. Photovolt. Res. Appl. **5**, 29–50 (1997)
5. J. Schmidt, J.D. Moschner, J. Henze, S. Dauwe, R. Hezel, Recent progress in the surface passivation of silicon solar cells using silicon nitride, in *Proc. 19th PVSEC* (2004), pp. 391–396
6. G. Dingemans, W.M.M. Kessels, Status and prospects of Al_2O_3-based surface passivation schemes for silicon solar cells. J. Vac. Sci. Technol. A **30**, 040802 (2012)
7. J. Schmidt, A. Merkle, R. Brendel, B. Hoex, M.C.M. van de Sanden, W.M.M. Kessels, Surface passivation of high-efficiency silicon solar cells by atomic-layer-deposited Al_2O_3. Prog. Photovolt. Res. Appl. **16**, 461–466 (2008)
8. M.A. Green, The passivated emitter and rear cell (PERC): from conception to mass production. Sol. Energy Mater. Sol. Cells **143**, 190–197 (2015)
9. S.W. Glunz, R. Preu, D. Biro, Crystalline silicon solar cells—state-of-the-art and future developments. Compr. Renew. Energy, Elsevier **1**, 353–387 (2012)
10. K. Wijekoon, F. Yan, Y. Zheng, D. Wang, H. Mungekar, L. Zhang, H. Ponnekanti, Optimization of rear local contacts on high efficiency PERC solar cells structures. Int. J. Photoenergy **2013**, 1–8 (2013)

11. F. Dross, K. Baert, T. Bearda, J. Deckers, V. Depauw, O. El Daif, I. Gordon, A. Gougam, J. Govaerts, S. Granata, R. Labie, X. Loozen, R. Martini, A. Masolin, B. O'Sullivan, Y. Qiu, J. Vaes, D. Van Gestel, J. Van Hoeymissen, A. Vanleenhove, K. Van Nieuwenhuysen, S. Venkatachalam, M. Meuris, J. Poortmans, Crystalline thin-foil silicon solar cells: where crystalline quality meets thin-film processing: crystalline quality meets thin-film processing. Prog. Photovolt. Res. Appl. **20**, 770–784 (2012)
12. P. Kapur, M. Moslehi, A. Deshpande, V. Rana, J. Kramer, S. Seutter, H. Deshazer, S. Coutant, A. Calcaterra, S. Kommera, S. Su, D. Grupp, S. Tamilmani, D. Dutton, T. Stalcup, T. Du, M. Wingert, A manufacturable, non-plated, non-Ag metallization based 20.44 % efficient, 243 cm^2 area, back contacted solar cell on 40 μm thick mono-crystalline silicon, in *Proc. 28th PVSEC* (2013), pp. 2228–2231
13. J.H. Petermann, D. Zielke, J. Schmidt, F. Haase, E.G. Rojas, R. Brendel, 19 %-Efficient and 43 μm-thick crystalline Si solar cell from layer transfer using porous silicon. Prog. Photovolt. Res. Appl. **20**, 1–5 (2012)
14. J. Govaerts, C. Trompoukis, H.S. Radhakrishnan, L. Tous, S.N. Granata, E.G. Carnemolla, R. Martini, A. Marchegiani, M. Karim, I. Sharlandziev, T. Bearda, V. Depauw, K. Van Nieuwenhuysen, I. Gordon, J. Szlufczik, J. Poortmans, Solar cells from epitaxial foils: an epifoil epiphany. Energy Procedia **77**, 871–880 (2015)
15. M.J. Kerr, P. Campbell, A. Cuevas, Lifetime and efficiency limits of crystalline silicon solar cells, in *Photovoltaic Specialists Conference (PVSC), 29th IEEE*, (2002), pp. 438–441
16. M.A. Green, Limiting efficiency of bulk and thin-film silicon solar cells in the presence of surface recombination. Prog. Photovolt. Res. Appl. **7**, 327–330 (1999)
17. A. Bozzola, P. Kowalczewski, L.C. Andreani, Towards high efficiency thin-film crystalline silicon solar cells: the roles of light trapping and non-radiative recombinations. J. Appl. Phys. **115**, 094501 (2014)
18. M. Taguchi, A. Yano, S. Tohoda, K. Matsuyama, Y. Nakamura, T. Nishiwaki, K. Fujita, E. Maruyama, 24.7 % Record efficiency HIT solar cell on thin silicon wafer. IEEE J. Photovolt. **4**, 96–99 (2014)
19. M. Bivour, C. Meinhardt, D. Pysch, C. Reichel, K.-U. Ritzau, M. Hermle, and S. W. Glunz, *n*-Type silicon solar cells with amorphous/crystalline silicon heterojunction rear emitter, in *Photovoltaic Specialists Conference (PVSC), 35th IEEE* (2010), pp. 001304–001308
20. L. Tous, S.N. Granata, P. Choulat, T. Bearda, A. Michel, A. Uruena, E. Cornagliotti, M. Aleman, R. Gehlhaar, R. Russell, F. Duerinckx, J. Szlufcik, Process simplifications in large area hybrid silicon heterojunction solar cells. Sol. Energy Mater. Sol. Cells **142**, 66–74 (2015)
21. I. Dirnstorfer, F. Benner, D. K. Simon, T. Mikolajick, N. Schilling, U. Klotzbach, Feasibility study for silicon heterojunction metal wrap through solar cells. *Proc. 28th PVSEC* (2013), pp. 1108–1112
22. S. De Wolf, A. Descoeudres, Z.C. Holman, C. Ballif, High-efficiency silicon heterojunction solar cells: a review. Green **2**, 7–24 (2012)
23. A.G. Aberle, S. Glunz, W. Warta, Impact of illumination level and oxide parameters on Shockley–Read–Hall recombination at the Si-SiO_2 interface. J. Appl. Phys. **71**, 4422 (1992)
24. M.J. Kerr, A. Cuevas, Very low bulk and surface recombination in oxidized silicon wafers. Semicond. Sci. Technol. **17**, 35–38 (2002)
25. S.W. Glunz, A.B. Sproul, W. Warta, W. Wettling, Injection-level-dependent recombination velocities at the Si-SiO_2 interface for various dopant concentrations. J. Appl. Phys. **75**, 1611 (1994)
26. K. Carstens, M. Dahlinger, E. Hoffmann, J.R. Köhler, R. Zapf-Gottwick, J.H. Werner, Universal passivation for p++ and n++ areas on IBC solar cells. Energy Procedia **77**, 779–785 (2015)
27. B.W.H. van de Loo, H.C.M. Knoops, G. Dingemans, G.J.M. Janssen, M.W.P.E. Lamers, I.G. Romijn, A.W. Weeber, W.M.M. Kessels, 'Zero-charge' SiO_2/Al_2O_3 stacks for the simultaneous passivation of n+ and p+ doped silicon surfaces by atomic layer deposition. Sol. Energy Mater. Sol. Cells **143**, 450–456 (2015)

28. U. Wurfel, A. Cuevas, P. Wurfel, Charge carrier separation in solar cells. IEEE J. Photovolt. **5**, 461–469 (2015)
29. C. Strümpel, M. McCann, G. Beaucarne, V. Arkhipov, A. Slaoui, V. Švrček, C. del Cañizo, I. Tobias, Modifying the solar spectrum to enhance silicon solar cell efficiency—an overview of available materials. Sol. Energy Mater. Sol. Cells **91**, 238–249 (2007)
30. W. Shockley, H.J. Queisser, Detailed balance limit of efficiency of *p-n* junction solar cells. J. Appl. Phys. **32**, 510 (1961)
31. T. Trupke, A. Shalav, B.S. Richards, P. Würfel, M.A. Green, Efficiency enhancement of solar cells by luminescent up-conversion of sunlight. Sol. Energy Mater. Sol. Cells **90**, 3327–3338 (2006)
32. W. Shockley, W.T. Read, Statistics of the recombinations of holes and electrons. Phys. Rev. **87**, 835–842 (1952)
33. R.N. Hall, Electron-hole recombination in germanium. Phys. Rev. **87**, 387 (1952)
34. D.K. Schroder, *Semiconductor material and device characterization*, 3rd edn. (N.J. IEEE Press. Wiley, Hoboken, 2006)
35. F. Werner, A. Cosceev, J. Schmidt, Interface recombination parameters of atomic-layer-deposited Al_2O_3 on crystalline silicon. J. Appl. Phys. **111**, 073710 (2012)
36. P. Saint-Cast, Y.-H. Heo, E. Billot, P. Olwal, M. Hofmann, J. Rentsch, S.W. Glunz, R. Preu, Variation of the layer thickness to study the electrical property of PECVD Al_2O_3/c-Si interface. Energy Procedia **8**, 642–647 (2011)
37. L.E. Black, K.R. McIntosh, Modeling recombination at the Si-Al_2O_3 interface. IEEE J. Photovolt. **3**, 936–943 (2013)
38. W.G.J.H.M. van Sark, L. Korte, F. Roca (eds.), *Physics and Technology of Amorphous-Crystalline Heterostructure Silicon Solar Cells* (Springer, Heidelberg, 2012)
39. T. Dullweber, M. Siebert, B. Veith, C. Kranz, J. Schmidt, R. Brendel, B. F. P. Roos, T. Dippell, A. Schwabedissen, and S. Peters, High-efficiency industrial-type PERC solar cells applying ICP AlO_x as rear passivation layer. *Proc. 27th PVSEC* (2012), pp. 672–675
40. B. Hoex, S.B.S. Heil, E. Langereis, M.C.M. van de Sanden, W.M.M. Kessels, Ultralow surface recombination of c-Si substrates passivated by plasma-assisted atomic layer deposited Al_2O_3. Appl. Phys. Lett. **89**, 042112 (2006)
41. H. Mäckel, R. Lüdemann, Detailed study of the composition of hydrogenated SiN_x layers for high-quality silicon surface passivation. J. Appl. Phys. **92**, 2602 (2002)
42. R.A. Sinton, A. Cuevas, M. Stuckings, Quasi-steady-state photoconductance, a new method for solar cell material and device characterization. in *Photovoltaic Specialists Conference (PVSC), 25th IEEE* (1996), pp. 457–460
43. A. Cuevas, R.A. Sinton, Prediction of the open-circuit voltage of solar cells from the steady-state photoconductance. Prog. Photovolt. Res. Appl. **5**, 79–90 (1997)
44. K. Dornich, T. Hahn, J.R. Niklas, Non destructive electrical defect characterisation and topography of silicon wafers and epitaxial layers. MRS Proc. **864**(E11), 2 (2005)
45. D. Kiliani, G. Micard, B. Steuer, B. Raabe, A. Herguth, G. Hahn, Minority charge carrier lifetime mapping of crystalline silicon wafers by time-resolved photoluminescence imaging. J. Appl. Phys. **110**, 054508 (2011)
46. A.B. Sproul, Dimensionless solution of the equation describing the effect of surface recombination on carrier decay in semiconductors. J. Appl. Phys. **76**, 2851 (1994)
47. A. Richter, S.W. Glunz, F. Werner, J. Schmidt, A. Cuevas, Improved quantitative description of Auger recombination in crystalline silicon. Phys. Rev. B **86**, 165202 (2012)
48. R.B.M. Girisch, R.P. Mertens, R.F. De Keersmaecker, Determination of Si-SiO_2 interface recombination parameters using a gate-controlled point-junction diode under illumination. IEEE Trans. Electron Devices **35**, 203–222 (1988)
49. D.A. Clugston, P.A. Basore, PC1D version 5: 32-bit solar cell modeling on personal computers, in *Proc. PVSC*, *26th IEEE* (1997), pp. 207–210
50. R. Stangl, C. Leendertz, J. Haschke, Numerical simulation of solar cells and solar cell characterization methods: the open-source on demand program AFORS-HET, in *InTech e-book: "SolarEnergy"* (2010)

51. S. Steingrube, P.P. Altermatt, D.S. Steingrube, J. Schmidt, R. Brendel, Interpretation of recombination at c-Si/SiN_x interfaces by surface damage. J. Appl. Phys. **108**, 014506 (2010)
52. B. Hoex, J.J.H. Gielis, M.C.M. van de Sanden, W.M.M. Kessels, On the c-Si surface passivation mechanism by the negative-charge-dielectric Al_2O_3. J. Appl. Phys. **104**, 113703 (2008)
53. J.R. Elmiger, Recombination at the silicon nitride/silicon interface. J. Vac. Sci. Technol. A **15**, 2418 (1997)
54. J. Schmidt, A.G. Aberle, Carrier recombination at silicon-silicon nitride interfaces fabricated by plasma-enhanced chemical vapor deposition. J. Appl. Phys. **85**, 3626 (1999)
55. G. Dingemans, N.M. Terlinden, M.A. Verheijen, M.C.M. van de Sanden, W.M.M. Kessels, Controlling the fixed charge and passivation properties of Si(100)/Al_2O_3 interfaces using ultrathin SiO_2 interlayers synthesized by atomic layer deposition. J. Appl. Phys. **110**, 093715 (2011)
56. S.W. Glunz, D. Biro, S. Rein, W. Warta, Field-effect passivation of the SiO_2-Si interface. J. Appl. Phys. **86**, 683 (1999)
57. S. Steingrube, P.P. Altermatt, D. Zielke, F. Werner, J. Schmidt, R. Brendel, Reduced passivation of silicon surfaces at low injection densities caused by H-induced defects, in *Proc. 15th PVSEC* (2010), pp. 1748–1754
58. F.-J. Ma, G.G. Samudra, M. Peters, A.G. Aberle, F. Werner, J. Schmidt, B. Hoex, Advanced modeling of the effective minority carrier lifetime of passivated crystalline silicon wafers. J. Appl. Phys. **112**, 054508 (2012)
59. Z. Hameiri, Fa-Jun Ma, K.R. McIntosh, Investigation of low injection effects using the local ideality factor obtained from effective lifetime measurements. *Photovoltaic Specialists Conference (PVSC), 2014 IEEE 40th*, pp. 1842–1847
60. I. Dirnstorfer, D.K. Simon, P.M. Jordan, T. Mikolajick, Near surface inversion layer recombination in Al_2O_3 passivated *n*-type silicon. J. Appl. Phys. **116**, 044112 (2014)
61. M. Kessler, T. Ohrdes, P.P. Altermatt, R. Brendel, The effect of sample edge recombination on the averaged injection-dependent carrier lifetime in silicon. J. Appl. Phys. **111**, 054508 (2012)
62. B. Veith, T. Ohrdes, F. Werner, R. Brendel, P.P. Altermatt, N.-P. Harder, J. Schmidt, Injection dependence of the effective lifetime of n-type Si passivated by Al_2O_3: An edge effect? Sol. Energy Mater. Sol. Cells **120**, 436–440 (2014)
63. J. Robertson, R.M. Wallace, High-K materials and metal gates for CMOS applications. Mater. Sci. Eng. R Rep. **88**, 1–41 (2015)
64. B.E. Deal, A.S. Grove, General relationship for the thermal oxidation of silicon. J. Appl. Phys. **36**, 3770 (1965)
65. B.E. Deal, M. Sklar, A.S. Grove, E.H. Snow, Characteristics of the surface-state charge (Q_{ss}) of thermally oxidized silicon. J. Electrochem. Soc. **114**, 266 (1967)
66. F.J. Himpsel, F.R. McFeely, A. Taleb-Ibrahimi, J.A. Yarmoff, G. Hollinger, Microscopic structure of the SiO_2/Si interface. Phys. Rev. B **38**, 6084–6096 (1988)
67. F. Werner, B. Veith, D. Zielke, L. Kühnemund, C. Tegenkamp, M. Seibt, R. Brendel, J. Schmidt, Electronic and chemical properties of the c-Si/Al_2O_3 interface. J. Appl. Phys. **109**, 113701 (2011)
68. F. Benner, P.M. Jordan, M. Knaut, I. Dirnstorfer, J.W. Bartha, T. Mikojajick, Investigation of the c-Si/Al_2O_3 interface for silicon surface passivation, in *Proc 27th PVSEC* (2012), pp. 1793–1796
69. M. Bhaisare, A. Misra, A. Kottantharayil, Aluminum oxide deposited by pulsed-DC reactive sputtering for crystalline slicon surface passivation. IEEE J. Photovolt. **3**, 930–935 (2013)
70. V. Verlaan, L.R.J.G. van den Elzen, G. Dingemans, M.C.M. van de Sanden, W.M.M. Kessels, Composition and bonding structure of plasma-assisted ALD Al_2O_3 films. Phys. Status Solidi C **7**, 976–979 (2010)
71. O. Renault, L.G. Gosset, D. Rouchon, A. Ermolieff, Angle-resolved x-ray photoelectron spectroscopy of ultrathin Al_2O_3 films grown by atomic layer deposition. J. Vac. Sci. Technol. A **20**, 1867 (2002)

72. F. Lin, B. Hoex, Y.H. Koh, J. Lin, A.G. Aberle, Low-temperature surface passivation of moderately doped crystalline silicon by atomic-layer-deposited hafnium oxide films. ECS J. Solid State Sci. Technol. **2**, N11–N14 (2012)
73. D.K. Simon, P.M. Jordan, M. Knaut, T. Chohan, T. Mikolajick, I. Dirnstorfer, ALD Al_2O_3 based Nanolaminates for Solar Cell Applications, in *Photovoltaic Specialists Conference (PVSC), IEEE 42th* (2015), pp. 1–6
74. A.G. Aberle, Overview on SiN surface passivation of crystalline silicon solar cells. Sol. Energy Mater. Sol. Cells **65**, 239–248 (2001)
75. A. Stesmans, V.V. Afanas'ev, Si dangling-bond-type defects at the interface of (100)Si with ultrathin layers of SiO_x, Al_2O_3, and ZrO_2. *Appl. Phys. Lett.* **80**, 1957 (2002)
76. G. Dingemans, M.C.M. van de Sanden, W.M.M. Kessels, Influence of the deposition temperature on the c-Si surface passivation by Al_2O_3 films synthesized by ALD and PECVD. Electrochem. Solid-State Lett. **13**, H76–H79 (2010)
77. M.D. Groner, F.H. Fabreguette, J.W. Elam, S.M. George, Low-temperature Al_2O_3 atomic layer deposition. Chem. Mater. **16**, 639–645 (2004)
78. J. Schmidt, M. Kerr, A. Cuevas, Surface passivation of silicon solar cells using plasma-enhanced chemical-vapour-deposited SiN films and thin thermal SiO_2/plasma SiN stacks. Semicond. Sci. Technol. **16**, 164–170 (2001)
79. G. Dingemans, C. Van Helvoirt, M.C.M. Van de Sanden, W.M. Kessels, Plasma-assisted atomic layer deposition of low temperature SiO_2. ECS Trans. **35**, 191–204 (2011)
80. G. Dingemans, W. Beyer, M.C.M. van de Sanden, W.M.M. Kessels, Hydrogen induced passivation of Si interfaces by Al_2O_3 films and SiO_2/Al_2O_3 stacks. Appl. Phys. Lett. **97**, 152106 (2010)
81. G. Dingemans, F. Einsele, W. Beyer, M.C.M. van de Sanden, W.M.M. Kessels, Influence of annealing and Al_2O_3 properties on the hydrogen-induced passivation of the Si/SiO_2 interface. J. Appl. Phys. **111**, 093713 (2012)
82. A. Richter, J. Benick, M. Hermle, S.W. Glunz, Reaction kinetics during the thermal activation of the silicon surface passivation with atomic layer deposited Al_2O_3. Appl. Phys. Lett. **104**, 061606 (2014)
83. X. Zhang, A. Thomson, A. Cuevas, Silicon surface passivation by sputtered aluminium oxide: influence of annealing temperature and ambient gas. ECS Solid State Lett. **3**, N37–N39 (2014)
84. A. Stesmans, Passivation of P_{b0} and P_{b1} interface defects in thermal (100) Si/SiO_2 with molecular hydrogen. Appl. Phys. Lett. **68**, 2076 (1996)
85. L. Tsetseris, S.T. Pantelides, Migration, incorporation, and passivation reactions of molecular hydrogen at the $Si\text{-}SiO_2$ interface. Phys. Rev. B **70**, 245320 (2004)
86. F. Kersten, A. Schmid, S. Bordihn, J.W. Müller, J. Heitmann, Role of annealing conditions on surface passivation properties of ALD Al_2O_3 films. Energy Procedia **38**, 843–848 (2013)
87. I. Dirnstorfer, T. Chohan, P.M. Jordan, M. Knaut, D.K. Simon, J.W. Bartha, T. Mikojajick, Al_2O_3–TiO_2 nanolaminates for conductive silicon surface passivation. IEEE J. Photovolt. **6**, 86–91 (2015)
88. N.M. Terlinden, G. Dingemans, M.C.M. van de Sanden, W.M.M. Kessels, Role of field-effect on c-Si surface passivation by ultrathin (2–20 nm) atomic layer deposited Al_2O_3. Appl. Phys. Lett. **96**, 112101 (2010)
89. B. Veith, F. Werner, D. Zielke, R. Brendel, J. Schmidt, Comparison of the thermal stability of single Al_2O_3 layers and Al_2O_3/SiN_x stacks for the surface passiviation of silicon. Energy Procedia **8**, 307–312 (2011)
90. W. Liang, K.J. Weber, A.F. Thomson, Effective SiN_x: H capping layers on 1-nm Al_2O_3 for p^+ Surface Passivation. IEEE J. Photovolt. **4**, 1405–1412 (2014)
91. D. Schuldis, A. Richter, J. Benick, P. Saint-Cast, M. Hermle, S.W. Glunz, Properties of the c-Si/Al_2O_3 interface of ultrathin atomic layer deposited Al_2O_3 layers capped by SiN_x for c-Si surface passivation. Appl. Phys. Lett. **105**, 231601 (2014)

92. P. Saint-Cast, D. Kania, R. Heller, S. Kuehnhold, M. Hofmann, J. Rentsch, R. Preu, High-temperature stability of c-Si surface passivation by thick PECVD Al_2O_3 with and without hydrogenated capping layers. Appl. Surf. Sci. **258**, 8371–8376 (2012)
93. S.M. Sze, K.K. Ng, *Physics of Semiconductor Devices*, 3rd edn (2007)
94. S. Duttagupta, F. Lin, K.D. Shetty, A.G. Aberle, B. Hoex, Excellent boron emitter passivation for high-efficiency Si wafer solar cells using AlO_x/SiN_x dielectric stacks deposited in an industrial inline plasma reactor: Excellent boron emitter passivation for high-efficiency Si wafer solar cells. Prog. Photovolt. Res. Appl. **21**, 760–764 (2012)
95. W. Liang, K.J. Weber, D. Suh, S.P. Phang, J. Yu, A.K. McAuley, B.R. Legg, Surface passivation of boron-diffused *p*-type silicon surfaces with (100) and (111) orientations by ALD Al_2O_3 layers. IEEE J. Photovolt. **3**, 678–683 (2013)
96. L.E. Black, T.C. Kho, K.R. McIntosh, A. Cuevas, The influence of orientation and morphology on the passivation of crystalline silicon surfaces by Al_2O_3. Energy Procedia **55**, 750–756 (2014)
97. H.C. Sio, S.P. Phang, Y. Wan, W. Liang, T. Trupke, S. Cao, D. Hu, Y. Wan, D. Macdonald, The influence of crystal orientation on surface passivation in multi-crystalline silicon, in *Photovoltaic Specialists Conference (PVSC), IEEE 39th* (2013), pp. 1770–1775
98. H. Haug, Ø. Nordseth, E.V. Monakhov, E.S. Marstein, Photoluminescence imaging under applied bias for characterization of Si surface passivation layers. Sol. Energy Mater. Sol. Cells **106**, 60–65 (2012)
99. P.M. Jordan, D.K. Simon, F.P.G. Fengler, T. Mikolajick, I. Dirnstorfer, 2D mapping of chemical and field effect passivation of Al_2O_3 on silicon substrates. Energy Procedia **77**, 91–98 (2015)
100. P.M. Jordan, D.K. Simon, T. Mikolajick, I. Dirnstorfer, BiasMDP: carrier lifetime characterization technique with applied bias voltage. Appl. Phys. Lett. **106**, 061602 (2015)
101. W.L. Warren, F.C. Rong, E.H. Poindexter, G.J. Gerardi, J. Kanicki, Structural identification of the silicon and nitrogen dangling-bond centers in amorphous silicon nitride. J. Appl. Phys. **70**, 346 (1991)
102. K.T. Butler, M.P.W.E. Lamers, A.W. Weeber, J.H. Harding, Molecular dynamics studies of the bonding properties of amorphous silicon nitride coatings on crystalline silicon. J. Appl. Phys. **110**, 124905 (2011)
103. S. Garcia, I. Martil, G. Gonzalez Diaz, E. Castan, S. Dueñas, M. Fernandez, Deposition of SiNx: H thin films by the electron cyclotron resonance and its application to Al/SiN_x:H/Si structures. J. Appl. Phys. **83**, 332 (1998)
104. G. Lucovsky, Defect properties of Si-, O-, N-, and H-atoms at Si—SiO_2 interfaces. J. Vac. Sci. Technol. B **14**, 2832 (1996)
105. G. Dingemans, N.M. Terlinden, D. Pierreux, H.B. Profijt, M.C.M. van de Sanden, W.M.M. Kessels, Influence of the oxidant on the chemical and field-effect passivation of Si by ALD Al_2O_3. Electrochem. Solid-State Lett. **14**, H1 (2011)
106. D.K. Simon, T. Henke, P.M. Jordan, F.P.G. Fengler, T. Mikolajick, J.W. Bartha, I. Dirnstorfer, Low-thermal budget flash light annealing for Al_2O_3 surface passivation: low-thermal budget flash light annealing for Al_2O_3 surface passivation. Phys. Status Solidi RRL—Rapid Res. Lett. **9**, 631–635 (2015)
107. D.K. Simon, Realization and characterization of advanced nanolayers for photovoltaic applications, PhD thesis, TU Dresden (2016)
108. J. Benick, A. Richter, T.-T.A. Li, N.E. Grant, K.R. McIntosh, Y. Ren, K.J. Weber, M. Hermle, S.W. Glunz, Effect of a post-deposition anneal on Al_2O_3/Si interface properties, in *Photovoltaic Specialists Conference (PVSC), IEEE 35th* (2010), pp. 000891–000896
109. D.K. Simon, P.M. Jordan, T. Mikolajick, I. Dirnstorfer, On the control of the fixed charge densities in Al_2O_3 based silicon surface passivation schemes. ACS Appl. Mater. Interfaces **7**, 28215–28222 (2015)
110. A. Rothschild, B. Vermang, X. Loozen, B.J. O'Sullivan, J. John, J. Poortmans, ALD-Al_2O_3 passivation for solar cells: charge investigation, in *Proc 25th PVSEC* (2010), pp. 1382–1385

111. B. Shin, J.R. Weber, R.D. Long, P.K. Hurley, C.G. Van de Walle, P.C. McIntyre, Origin and passivation of fixed charge in atomic layer deposited aluminum oxide gate insulators on chemically treated InGaAs substrates. Appl. Phys. Lett. **96**, 152908 (2010)
112. Y. Ahn, S.H. Choudhury, D. Lee, S.M. Sadaf, M. Siddik, M. Jo, S. Park, Y.D. Kim, D.H. Kim, H. Hwang, Estimation of interfacial fixed charge at Al_2O_3/SiO_2 using Slant-Etched wafer for solar cell application. Jpn. J. Appl. Phys. **50**, 071503 (2011)
113. V. Naumann, M. Otto, R.B. Wehrspohn, C. Hagendorf, Chemical and structural study of electrically passivating Al_2O_3/Si interfaces prepared by atomic layer deposition. J. Vac. Sci. Technol. A **30**, 04D106 (2012)
114. K. Kimoto, Y. Matsui, T. Nabatame, T. Yasuda, T. Mizoguchi, I. Tanaka, A. Toriumi, Coordination and interface analysis of atomic-layer-deposition Al_2O_3 on Si(001) using energy-loss near-edge structures. Appl. Phys. Lett. **83**, 4306 (2003)
115. G. Lucovsky, A chemical bonding model for the native oxides of the III–V compound semiconductors. J. Vac. Sci. Technol. **19**, 456 (1981)
116. K. Matsunaga, T. Tanaka, T. Yamamoto, Y. Ikuhara, First-principles calculations of intrinsic defects in Al_2O_3. Phys. Rev. B **68**, 085110 (2003)
117. J.R. Weber, A. Janotti, C.G. Van de Walle, Native defects in Al_2O_3 and their impact on III-V/Al_2O_3 metal-oxide-semiconductor-based devices. J. Appl. Phys. **109**, 033715 (2011)
118. M. Choi, A. Janotti, C.G. Van de Walle, Native point defects and dangling bonds in α-Al_2O_3. J. Appl. Phys. **113**, 044501 (2013)
119. J.J.H. Gielis, B. Hoex, M.C.M. van de Sanden, W.M.M. Kessels, Negative charge and charging dynamics in Al_2O_3 films on Si characterized by second-harmonic generation. J. Appl. Phys. **104**, 073701 (2008)
120. B. Liao, R. Stangl, T. Mueller, F. Lin, C.S. Bhatia, B. Hoex, The effect of light soaking on crystalline silicon surface passivation by atomic layer deposited Al_2O_3. J. Appl. Phys. **113**, 024509 (2013)
121. J.A. Töfflinger, A. Laades, C. Leendertz, L.M. Montañez, L. Korte, U. Stürzebecher, H.-P. Sperlich, B. Rech, PECVD-AlO_x/SiN_x passivation stacks on silicon: effective charge dynamics and interface defect state spectroscopy. Energy Procedia **55**, 845–854 (2014)
122. F. Benner, M. Knaut, P.M. Jordan, I. Dirnstorfer, J. Ocker, J.W. Bartha, T. Mikolajick, Improvement of Al_2O_3 passivation by Ti-doping, in *Proc 28th PVSEC* (2013), pp. 1156–1161
123. F. Werner, J. Schmidt, Manipulating the negative fixed charge density at the c-Si/Al_2O_3 interface. Appl. Phys. Lett. **104**, 091604 (2014)
124. M. Cho, R. Degraeve, P. Roussel, B. Govoreanu, B. Kaczer, M.B. Zahid, E. Simoen, A. Arreghini, M. Jurczak, J.V. Houdt, G. Groeseneken, A consistent model for oxide trap profiling with the trap spectroscopy by charge injection and sensing (TSCIS) technique. Solid-State Electron. **54**, 1384–1391 (2010)
125. E. Vianello, F. Driussi, A. Arreghini, P. Palestri, D. Esseni, L. Selmi, N. Akil, M.J. van Duuren, D.S. Golubovic, Experimental and simulation analysis of program/retention transients in silicon nitride-based NVM cells. IEEE Trans. Electron Devices **56**, 1980–1990 (2009)
126. T. Mikolajick, M. Specht, N. Nagel, T. Mueller, S. Riedel, F. Beug, T. Melde, K.-H. Kusters, The future of charge trapping memories. Int. Symp. VLSI-TSA **2007**, 1–4 (2007)
127. N.M. Terlinden, G. Dingemans, V. Vandalon, R.H.E.C. Bosch, W.M.M. Kessels, Influence of the SiO_2 interlayer thickness on the density and polarity of charges in Si/SiO_2/Al_2O_3 stacks as studied by optical second-harmonic generation. J. Appl. Phys. **115**, 033708 (2014)
128. R. Degraeve, M. Cho, B. Govoreanu, B. Kaczer, M.B. Zahid, J. Van Houdt, M. Jurczak, G. Groeseneken, Trap spectroscopy by charge injection and sensing (TSCIS): a quantitative electrical technique for studying defects in dielectric stacks (IEDM, IEEE Int. Electron Devices Meet, 2008), pp. 775–778
129. M. Toledano-Luque, R. Degraeve, M.B. Zahid, B. Kaczer, J. Kittl, M. Jurczak, G. Groeseneken, J. Van Houdt, Resolving fast VTH transients after program/erase of flash memory stacks and their relation to electron and hole defects (IEDM, IEEE Int. Electron Devices Meet, 2009), pp. 749–752

130. M. Bazilchuk, H. Haug, E.S. Marstein, Modulating the fixed charge density in silicon nitride films while monitoring the surface recombination velocity by photoluminescence imaging. Appl. Phys. Lett. **106**, 143505 (2015)
131. Y. Ren, K. Weber, F. Karouta, K. Vora, W. Liang, Charge trapping and storage in SiN_x thin films deposited with Oxford PlasmaLab 100 system, in *Photovoltaic Specialists Conference (PVSC), 38th IEEE* (2012), pp. 001094–001097
132. www.itrpv.net, "International Technology Roadmap for Photovoltaic (ITRPV), 2014 Results," 01-Jul-2015
133. S. Miyajima, J. Irikawa, A. Yamada, M. Konagai, High quality aluminum oxide passivation layer for crystalline silicon solar cells deposited by parallel-plate plasma-enhanced chemical vapor deposition. Appl. Phys. Express **3**, 012301 (2010)
134. T. Lauinger, Optimization and characterization of remote plasma-enhanced chemical vapor deposition silicon nitride for the passivation of *p*-type crystalline silicon surfaces. J. Vac. Sci. Technol. A **16**, 530 (1998)
135. Y. Wan, K.R. McIntosh, A.F. Thomson, A. Cuevas, Low surface recombination velocity by low-absorption silicon nitride on c-Si. IEEE J. Photovolt. **3**, 554–559 (2013)
136. S. Duttagupta, F. Ma, B. Hoex, T. Mueller, A.G. Aberle, Optimised antireflection coatings using silicon nitride on textured silicon surfaces based on measurements and multidimensional modelling. Energy Procedia **15**, 78–83 (2012)
137. Z. Hameiri, L. Mai, N. Borojevic, S. Javid, B. Tjahjono, S. Wang, A. Sproul, S. Wenham, The influence of silicon nitride layer parameters on the implied Voc of CZ silicon wafers after annealing, in *Photovoltaic Specialists Conference (PVSC), 34th IEEE* (2009), pp. 1795–1800
138. M. Hofmann, S. Kambor, C. Schmidt, D. Grambole, J. Rentsch, S. W. Glunz, R. Preu, PECVD-ONO: a new deposited firing stable rear surface passivation layer system for crystalline silicon solar cells. Adv. Optoelectron., 1–10 (2008)
139. Z. Chen, S.K. Pang, K. Yasutake, A. Rohatgi, Plasma-enhanced chemical-vapor-deposited oxide for low surface recombination velocity and high effective lifetime in silicon. J. Appl. Phys. **74**, 2856 (1993)
140. J. Irikawa, S. Miyajima, S. Kida, T. Watahiki, M. Konagai, Effects of annealing and atomic hydrogen treatment on aluminum oxide passivation layers for crystalline silicon solar cells. Jpn. J. Appl. Phys. **50**, 012301 (2011)
141. G. Dingemans, P. Engelhart, R. Seguin, M.M. Mandoc, M.C.M. van de Sanden, W.M.M. Kessels, Comparison between aluminum oxide surface passivation films deposited with thermal ALD, plasma ALD and PECVD, in *Photovoltaic Specialists Conference (PVSC), 35th IEEE* (2010), pp. 003118–003121
142. H.-P. Sperlich, D. Decker, P. Saint-Cast, E. Erben, L. Peters, High productive solar cell passivation on Roth&Rau MAiA® MW-PECVD Inline machine—a comparison of Al_2O_3, SiO_2 and SiN_x-H process conditions and performance. in *Proc 25th PVSEC* (2010), pp. 1352–1357
143. P. Saint-Cast, D. Kania, M. Hofmann, J. Benick, J. Rentsch, R. Preu, Very low surface recombination velocity on *p*-type c-Si by high-rate plasma-deposited aluminum oxide. Appl. Phys. Lett. **95**, 151502 (2009)
144. A. Laades, H.-P. Sperlich, M. Bähr, U. Stürzebecher, C.A. Diaz Alvarez, M. Burkhardt, H. Angermann, M. Blech, A. Lawerenz, On the impact of interfacial SiO_x-layer on the passivation properties of PECVD synthesized aluminum oxide: on the impact of interfacial SiO_x-layer on the passivation properties of PECVD synthesized aluminum oxide. Phys. Status Solidi C **9**, 2120–2123 (2012)
145. M.D. Groner, S.M. George, High-k dielectrics grown by atomic layer deposition. *Interlayer Dielectrics for Semiconductor Technologies* (Elsevier, Amsterdam, 2003), pp. 327–348
146. S.M. George, Atomic layer deposition: an overview. Chem. Rev. **110**, 111–131 (2010)
147. G. Agostinelli, A. Delabie, P. Vitanov, Z. Alexieva, H.F.W. Dekkers, S. De Wolf, G. Beaucarne, Very low surface recombination velocities on *p*-type silicon wafers passivated with a dielectric with fixed negative charge. Sol. Energy Mater. Sol. Cells **90**, 3438–3443 (2006)

148. H.C.M. Knoops, E.M.J. Braeken, K. de Peuter, S.E. Potts, S. Haukka, V. Pore, W.M.M. Kessels, Atomic layer deposition of silicon nitride from bis(tert-butylamino)silane and N_2 Plasma. ACS Appl. Mater. Interfaces **7**, 19857–19862 (2015)
149. S.W. King, Plasma enhanced atomic layer deposition of SiN_x: H and SiO_2. J. Vac. Sci. Technol. A **29**, 041501 (2011)
150. F. Werner, B. Veith, V. Tiba, P. Poodt, F. Roozeboom, R. Brendel, J. Schmidt, Very low surface recombination velocities on *p*- and *n*-type c-Si by ultrafast spatial atomic layer deposition of aluminum oxide. Appl. Phys. Lett. **97**, 162103 (2010)
151. F. Benner, P.M. Jordan, C. Richter, D.K. Simon, I. Dirnstorfer, M. Knaut, J.W. Bartha, T. Mikolajick, Atomic layer deposited high-κ nanolaminates for silicon surface passivation. J. Vac. Sci. Technol. B **32**, 03D110 (2014)
152. S. Bordihn, V. Mertens, J.W. Müller, W.M.M. Kessels, Deposition temperature dependence of material and Si surface passivation properties of O_3-based atomic layer deposited Al_2O_3-based films and stacks. J. Vac. Sci. Technol. A **32**, 01A128 (2014)
153. D.K. Simon, P.M. Jordan, I. Dirnstorfer, F. Benner, C. Richter, T. Mikolajick, Symmetrical Al_2O_3-based passivation layers for *p*- and *n*-type silicon. Sol. Energy Mater. Sol. Cells **131**, 72–76 (2014)
154. G. Dingemans, W.M.M. Kessels, Aluminum oxide and other ALD materials for Si surface passivation. ECS Trans. **41**, 293–301 (2011)
155. B. Liao, B. Hoex, A.G. Aberle, D. Chi, C.S. Bhatia, Excellent c-Si surface passivation by low-temperature atomic layer deposited titanium oxide. Appl. Phys. Lett. **104**, 253903 (2014)
156. D. Suh, D.-Y. Choi, K.J. Weber, Al_2O_3/TiO_2 stack layers for effective surface passivation of crystalline silicon. J. Appl. Phys. **114**, 154107 (2013)
157. Y. Wan, J. Bullock, A. Cuevas, Passivation of c-Si surfaces by ALD tantalum oxide capped with PECVD silicon nitride. Sol. Energy Mater. Sol. Cells **142**, 42–46 (2015)
158. T.G. Allen, M. Ernst, C. Samundsett, A. Cuevas, Demonstration of c-Si solar cells with gallium oxide surface passivation and laser-doped gallium p^+ regions. IEEE J. Photovolt. **5**, 1586–1590 (2015)
159. P. Poodt, D.C. Cameron, E. Dickey, S.M. George, V. Kuznetsov, G.N. Parsons, F. Roozeboom, G. Sundaram, A. Vermeer, Spatial atomic layer deposition: a route towards further industrialization of atomic layer deposition. J. Vac. Sci. Technol. A **30**, 010802 (2012)
160. V.I. Kuznetsov, M.A. Ernst, E.H.A. Granneman, Al_2O_3 surface passivation of silicon solar cells by low cost ald technology, in *Photovoltaic Specialists Conference (PVSC), IEEE 40th* (2014), pp. 0608–0611
161. E. Cornagliotti, L. Tous, A. Uruena de Castro, A. Rothschild, R. Russell, V. Lu, S. Radosavjlevic, J. John, J. Toman, M. Aleman, F. Duerinckx, J. Poortmans, J. Szlufcik, B. Dielissen, F. Souren, X. Gay, R. Görtzen, B. Hallam, Integration of spatial ALD aluminum oxide for rear side passivation of *p*-type PERC/PERL solar cells, in *Proc 28th PVSEC* (2013), pp. 976–981
162. L. Black, T. Allen, K.R. McIntosh, Safe and inexpensive Al_2O_3 deposited by APCVD with single-source precursor. *Proc 28th PVSEC* (2013), pp. 1068–1072
163. L.E. Black, K.R. McIntosh, Surface passivation of c-Si by atmospheric pressure chemical vapor deposition of Al_2O_3. Appl. Phys. Lett. **100**, 202107 (2012)
164. L.E. Black, T. Allen, A. Cuevas, K.R. McIntosh, B. Veith, J. Schmidt, Thermal stability of silicon surface passivation by APCVD Al_2O_3. Sol. Energy Mater. Sol. Cells **120**, 339–345 (2014)
165. A.F. Thomson, K.R. McIntosh, Light-enhanced surface passivation of TiO_2-coated silicon: light-enhanced surface passivation of TiO_2-coated silicon. Prog. Photovolt. Res. Appl. **20**, 343–349 (2012)
166. B.S. Richards, J.E. Cotter, C.B. Honsberg, Enhancing the surface passivation of TiO_2 coated silicon wafers. Appl. Phys. Lett. **80**, 1123 (2002)
167. M. Vetter, Surface passivation of silicon by rf magnetron-sputtered silicon nitride films. Thin Solid Films **337**, 118–122 (1999)

168. X. Zhang, A. Cuevas, Plasma hydrogenated, reactively sputtered aluminium oxide for silicon surface passivation. Phys. Status Solidi RRL—Rapid Res. Lett. **7**, 619–622 (2013)
169. T.-T.A. Li, A. Cuevas, Role of hydrogen in the surface passivation of crystalline silicon by sputtered aluminum oxide. Prog. Photovolt. Res. Appl. **19**, 320–325 (2011)
170. X. Zhang, A. Cuevas, A. Thomson, Process control of reactive sputter deposition of AlO_x and improved surface passivation of crystalline silicon. IEEE J. Photovolt. **3**, 183–188 (2013)
171. J. Schmidt, F. Werner, B. Veith, D. Zielke, S. Steingrube, P.P. Altermatt, S. Gatz, T. Dullweber, R. Brendel, Advances in the surface passivation of silicon solar cells. Energy Procedia **15**, 30–39 (2012)
172. S. Vandana, N. Batra, J. Gope, R. Singh, J. Panigrahi, S. Tyagi, P. Pathi, S.K. Srivastava, C. M.S. Rauthan, P.K. Singh, Effect of low thermal budget annealing on surface passivation of silicon by ALD based aluminum oxide films. Phys. Chem. Chem. Phys. **16**, 21804–21811 (2014)
173. G. Seguini, E. Cianci, C. Wiemer, D. Saynova, J.A.M. van Roosmalen, M. Perego, Si surface passivation by Al_2O_3 thin films deposited using a low thermal budget atomic layer deposition process. Appl. Phys. Lett. **102**, 131603 (2013)
174. T. Gebel, M. Voelskow, W. Skorupa, G. Mannino, V. Privitera, F. Priolo, E. Napolitani, A. Carnera, Flash lamp annealing with millisecond pulses for ultra-shallow boron profiles in silicon, Nucl. Instrum. Methods Phys. Res. Sect. B **186**, 287–291 (2002)
175. J. Lehmann, R. Hübner, J.V. Borany, W. Skorupa, T. Mikolajick, A. Schäfer, J. Schubert, S. Mantl, Millisecond flash lamp annealing for $LaLuO_3$ and $LaScO_3$ high-k dielectrics. Microelectron. Eng. **109**, 381–384 (2013)
176. T. Henke, M. Knaut, C. Hossbach, M. Geidel, L. Rebohle, M. Albert, W. Skorupa, J.W. Bartha, Flash-enhanced atomic layer deposition: basics, opportunities, review, and principal studies on the flash-enhanced growth of thin films. ECS J. Solid State Sci. Technol. **4**, P277–P287 (2015)
177. T. Gebel, L. Rebohle, R. Fendler, W. Hentsch, W. Skorupa, M. Voelskow, W. Anwand, R.A. Yankov, Millisecond annealing with flashlamps: Tool and process challenges, in RTP '06. 14th IEEE International Conference on Advanced Thermal Processing of Semiconductors (2006), pp. 47–55
178. R.A. McMahon, M.P. Smith, K.A. Seffen, M. Voelskow, W. Anwand, W. Skorupa, Flash-lamp annealing of semiconductor materials—applications and process models. Vacuum **81**, 1301–1305 (2007)
179. G. Dingemans, M.C.M. van de Sanden, W.M.M. Kessels, Excellent Si surface passivation by low temperature SiO_2 using an ultrathin Al_2O_3 capping film. Phys. Status Solidi RRL—Rapid Res. Lett. **5**, 22–24 (2011)
180. O. Sharia, A.A. Demkov, G. Bersuker, B.H. Lee, Effects of aluminum incorporation on band alignment at the SiO_2/HfO_2 interface. Phys. Rev. B **77**, 085326 (2008)
181. F. Feldmann, M. Bivour, C. Reichel, M. Hermle, S.W. Glunz, Passivated rear contacts for high-efficiency *n*-type Si solar cells providing high interface passivation quality and excellent transport characteristics. Sol. Energy Mater. Sol. Cells **120**, 270–274 (2014)
182. B. Nemeth, D.L. Young, H.-C. Yuan, V. LaSalvia, A.G. Norman, M. Page, B.G. Lee, P. Stradins, Low temperature Si/SiO_x/pc-Si passivated contacts to *n*-type Si solar cells, in *Photovoltaic Specialists Conference (PVSC), IEEE 40th* (2014), pp. 3448–3452
183. U. Römer, R. Peibst, T. Ohrdes, B. Lim, J. Krügener, E. Bugiel, T. Wietler, R. Brendel, Recombination behavior and contact resistance of n^+ and p^+ poly-crystalline Si/mono-crystalline Si junctions. Sol. Energy Mater. Sol. Cells **131**, 85–91 (2014)
184. D. Garcia-Alonso, S. Smit, S. Bordihn, W.M.M. Kessels, Silicon passivation and tunneling contact formation by atomic layer deposited Al_2O_3/ZnO stacks. Semicond. Sci. Technol. **28**, 082002 (2013)
185. D. Zielke, J.H. Petermann, F. Werner, B. Veith, R. Brendel, J. Schmidt, Contact passivation in silicon solar cells using atomic-layer-deposited aluminum oxide layers. Phys. Status Solidi RRL—Rapid Res. Lett. **5**, 298–300 (2011)

186. F. Feldmann, K.-U. Ritzau, M. Bivour, A. Moldovan, S. Modi, J. Temmler, M. Hermle, S.W. Glunz, High and low work function materials for passivated contacts. Energy Procedia **77**, 263–270 (2015)
187. H. Steinkemper, F. Feldmann, M. Bivour, M. Hermle, Numerical simulation of carrier-selective electron contacts featuring tunnel oxides. IEEE J. Photovolt. **5**, 1348–1356 (2015)
188. F. Klow, E.S. Marstein, S.E. Foss, Tunneling contact passivation simulations using Silvaco Atlas. Energy Procedia **77**, 99–105 (2015)
189. J.B. Heng, J. Fu, B. Kong, Y. Chae, W. Wang, Z. Xie, A. Reddy, K. Lam, C. Beitel, C. Liao, C. Erben, Z. Huang, Z. Xu, >23 % High-efficiency tunnel oxide junction bifacial solar cell with electroplated Cu gridlines. IEEE J. Photovolt. **5**, 82–86 (2015)
190. F. Feldmann, M. Bivour, C. Reichel, H. Steinkemper, M. Hermle, S.W. Glunz, Tunnel oxide passivated contacts as an alternative to partial rear contacts. Sol. Energy Mater. Sol. Cells **131**, 46–50 (2014)
191. B.G. Lee, J. Skarp, V. Malinen, S. Li, S. Choi, and H.M. Branz, Excellent passivation and low reflectivity Al_2O_3/TiO_2 bilayer coatings for *n*-wafer silicon solar cells, in *Photovoltaic Specialists Conference (PVSC), 38th IEEE* (2012), pp. 001066–001068
192. W.-C. Wang, M.-C. Tsai, J. Yang, C. Hsu, M.-J. Chen, Efficiency enhancement of nanotextured black silicon solar cells using Al_2O_3/TiO_2 dual-layer passivation stack prepared by atomic layer deposition. ACS Appl. Mater. Interfaces **7**, 10228–10237 (2015)
193. W. Jeon, H.-S. Chung, D. Joo, S.-W. Kang, $TiO_2/Al_2O_3/TiO_2$ nanolaminated thin films for DRAM capacitor deposited by Plasma-enhanced atomic layer deposition. Electrochem. Solid-State Lett. **11**, H19 (2008)
194. L. Aarik, T. Arroval, R. Rammula, H. Mändar, V. Sammelselg, B. Hudec, K. Hušeková, K. Fröhlich, J. Aarik, Atomic layer deposition of high-quality Al_2O_3 and Al-doped TiO_2 thin films from hydrogen-free precursors. Thin Solid Films **565**, 19–24 (2014)
195. W.D. Kim, G.W. Hwang, O.S. Kwon, S.K. Kim, M. Cho, D.S. Jeong, S.W. Lee, M.H. Seo, C.S. Hwang, Y.-S. Min, Y.J. Cho, Growth characteristics of atomic layer deposited TiO_2 thin films on Ru and Si electrodes for memory capacitor applications. J. Electrochem. Soc. **152**, C552 (2005)
196. I. Dirnstorfer, H. Mähne, T. Mikolajick, M. Knaut, M. Albert, K. Dubnack, Atomic layer deposition of anatase TiO_2 on porous electrodes for dye-sensitized solar cells. J. Vac. Sci. Technol. A **31**, 01A116 (2013)
197. R. Peibst, U. Romer, K.R. Hofmann, B. Lim, T.F. Wietler, J. Krugener, N.-P. Harder, R. Brendel, Simple model describing the symmetric I-V characteristics of *p* polycrystalline Si/*n* monocrystalline Si, and *n* polycrystalline Si/*p* monocrystalline Si junctions. IEEE J. Photovolt. **4**, 841–850 (2014)
198. E. Hecht, *Optics*, 4th edn (2014)
199. M.H. Kang, K. Ryu, A. Upadhyaya, A. Rohatgi, Optimization of SiN AR coating for Si solar cells and modules through quantitative assessment of optical and efficiency loss mechanism. Prog. Photovolt. Res. Appl. **19**, 983–990 (2011)
200. H. Nagel, A.G. Aberle, R. Hezel, Optimised antireflection coatings for planar silicon solar cells using remote PECVD silicon nitride and porous silicon dioxide. Prog. Photovolt. Res. Appl. **7**, 245–260 (1999)
201. E. Bustarret, M. Bensouda, M.C. Habrard, J.C. Bruyère, S. Poulin, S.C. Gujrathi, Configurational statistics in a-$Si_xN_yH_z$ alloys: a quantitative bonding analysis. Phys. Rev. B **38**, 8171–8184 (1988)
202. A. Thomson, Y. Wan, N. Lal, R.G. Elliman, Graded silicon nitride films: optics and passivation. J. Vac. Sci. Technol. A **33**, 060610 (2015)
203. S.W. Glunz, High-efficiency crystalline silicon solar cells. Adv. Optoelectron. 1–15 (2007)
204. D. Kray, M. Hermle, S.W. Glunz, Theory and experiments on the back side reflectance of silicon wafer solar cells. Prog. Photovolt. Res. Appl. **16**, 1–15 (2008)
205. J. Rentsch, H.-P. Sperlich, N. Kohn, D. Kania, P. Saint-Cast, S. Schetter, M. Hofmann, R. Preu, Industrial deposition of PECVD AlO_x for rear passivation of PERC type mc-Si solar cells, in *Proc 25th PVSEC*, pp. 1715–1718 (2010)

206. E. Yablonovitch, Statistical ray optics. J. Opt. Soc. Am. **72**, 899 (1982)
207. P. Campbell, M.A. Green, Light trapping properties of pyramidally textured surfaces. J. Appl. Phys. **62**, 243 (1987)
208. H. Seidel, Anisotropic etching of crystalline silicon in alkaline solutions. J. Electrochem. Soc. **137**, 3612–3626 (1990)
209. M. Otto, M. Algasinger, H. Branz, B. Gesemann, T. Gimpel, K. Füchsel, T. Käsebier, S. Kontermann, S. Koynov, X. Li, V. Naumann, J. Oh, A.N. Sprafke, J. Ziegler, M. Zilk, R.B. Wehrspohn, Black silicon photovoltaics. Adv. Opt. Mater. **3**, 147–164 (2015)
210. R. Einhaus, E. Vazsonyi, J. Szlufcik, J. Nijs, and R. Mertens, Isotropic texturing of multicrystalline silicon wafers with acidic texturing solutions, in *Photovoltaic Specialists Conference (PVSC), 26th IEEE* (1997), pp. 167–170
211. K. Kim, S.K. Dhungel, S. Jung, D. Mangalaraj, J. Yi, Texturing of large area multi-crystalline silicon wafers through different chemical approaches for solar cell fabrication. Sol. Energy Mater. Sol. Cells **92**, 960–968 (2008)
212. M. Burresi, F. Pratesi, F. Riboli, D.S. Wiersma, Complex photonic structures for light harvesting. Adv. Opt. Mater. **3**, 722–743 (2015)
213. C. Trompoukis, I. Abdo, R. Cariou, I. Cosme, W. Chen, O. Deparis, A. Dmitriev, E. Drouard, M. Foldyna, E.G. Caurel, I. Gordon, B. Heidari, A. Herman, L. Lalouat, K.-D. Lee, J. Liu, K. Lodewijks, F. Mandorlo, I. Massiot, A. Mayer, V. Mijkovic, J. Muller, R. Orobtchouk, G. Poulain, P. Prod'Homme, P.R. i Cabarrocas, C. Seassal, J. Poortmans, R. Mertens, O.E. Daif, V. Depauw, Photonic nanostructures for advanced light trapping in thin crystalline silicon solar cells: advanced light trapping in thin crystalline silicon solar cells. Phys. Status Solidi A **212**, 140–155 (2015)
214. Z. Yu, A. Raman, S. Fan, Fundamental limit of nanophotonic light trapping in solar cells. Proc. Natl. Acad. Sci. **107**, 17491–17496 (2010)
215. A. Mellor, I. Tobías, A. Martí, M.J. Mendes, A. Luque, Upper limits to absorption enhancement in thick solar cells using diffraction gratings. Prog. Photovolt. Res. Appl. **19**, 676–687 (2011)
216. K.X. Wang, Z. Yu, V. Liu, Y. Cui, S. Fan, Absorption enhancement in ultrathin crystalline silicon solar cells with antireflection and light-trapping nanocone gratings. Nano Lett. **12**, 1616–1619 (2012)
217. C. Trompoukis, O. El Daif, V. Depauw, I. Gordon, J. Poortmans, Photonic assisted light trapping integrated in ultrathin crystalline silicon solar cells by nanoimprint lithography. Appl. Phys. Lett. **101**, 103901 (2012)
218. N. Tucher, J. Eisenlohr, H. Hauser, J. Benick, M. Graf, C. Müller, M. Hermle, J.C. Goldschmidt, B. Bläsi, Crystalline silicon solar cells with enhanced light trapping via rear side diffraction grating. Energy Procedia **77**, 253–262 (2015)
219. M. Peters, M. Rüdiger, H. Hauser, M. Hermle, B. Bläsi, Diffractive gratings for crystalline silicon solar cells-optimum parameters and loss mechanisms: diffractive gratings for crystalline silicon solar cells. Prog. Photovolt. Res. Appl. **20**, 862–873 (2012)
220. R. Rothemund, T. Umundum, G. Meinhardt, K. Hingerl, T. Fromherz, W. Jantsch, Light trapping in pyramidally textured crystalline silicon solar cells using back-side diffractive gratings: Diffractive gratings for pyramidally textured silicon solar cells. Prog. Photovolt. Res. Appl. **21**, 747–753 (2012)
221. J. Eisenlohr, B.G. Lee, J. Benick, F. Feldmann, M. Drießen, N. Milenkovic, B. Bläsi, J.C. Goldschmidt, M. Hermle, Rear side sphere gratings for improved light trapping in crystalline silicon single junction and silicon-based tandem solar cells. Sol. Energy Mater. Sol. Cells **142**, 60–65 (2015)
222. J. Eisenlohr, J. Benick, M. Peters, B. Bläsi, J.C. Goldschmidt, M. Hermle, Hexagonal sphere gratings for enhanced light trapping in crystalline silicon solar cells. Opt. Express **22**, A111–A119 (2014)
223. X. Huang, S. Han, W. Huang, X. Liu, Enhancing solar cell efficiency: the search for luminescent materials as spectral converters. Chem. Soc. Rev. **42**, 173–201 (2013)

224. A. Shalav, B.S. Richards, M.A. Green, Luminescent layers for enhanced silicon solar cell performance: up-conversion. Sol. Energy Mater. Sol. Cells **91**, 829–842 (2007)
225. S. Fischer, J.C. Goldschmidt, P. Löper, G.H. Bauer, R. Brüggemann, K. Krämer, D. Biner, M. Hermle, S.W. Glunz, Enhancement of silicon solar cell efficiency by upconversion: optical and electrical characterization. J. Appl. Phys. **108**, 044912 (2010)
226. F. Lahoz, C. Pérez-Rodríguez, S.E. Hernández, I.R. Martín, V. Lavín, U.R. Rodríguez-Mendoza, Upconversion mechanisms in rare-earth doped glasses to improve the efficiency of silicon solar cells. Sol. Energy Mater. Sol. Cells **95**, 1671–1677 (2011)
227. B.S. Richards, A. Shalav, Enhancing the near-infrared spectral response of silicon optoelectronic devices via up-conversion. IEEE Trans. Electron Devices **54**, 2679–2684 (2007)
228. G.E. Arnaoutakis, J. Marques-Hueso, A. Ivaturi, S. Fischer, J.C. Goldschmidt, K.W. Krämer, B.S. Richards, Enhanced energy conversion of up-conversion solar cells by the integration of compound parabolic concentrating optics. Sol. Energy Mater. Sol. Cells **140**, 217–223 (2015)
229. G.H. Dieke, H.M. Crosswhite, The spectra of the doubly and triply ionized rare earths. Appl. Opt. **2**, 675 (1963)
230. J.C. Goldschmidt, S. Fischer, B. Herter, B. Fröhlich, K.W. Krämer, B.S. Richards, A. Ivaturi, S.K. . MacDougall, J. Marques Hueso, E. Favilla, M. Tonelli, Record efficient upconverter solar cell devices, in *Proc 29th PVSEC* (2014), pp. 1–4
231. S. Fischer, B. Fröhlich, H. Steinkemper, K.W. Krämer, J.C. Goldschmidt, Absolute upconversion quantum yield of β-NaYF4 doped with Er^{3+} and external quantum efficiency of upconverter solar cell devices under broad-band excitation considering spectral mismatch corrections. Sol. Energy Mater. Sol. Cells **122**, 197–207 (2014)
232. P.-A. Hansen, H. Fjellvåg, T. Finstad, O. Nilsen, Structural and optical properties of lanthanide oxides grown by atomic layer deposition (Ln = Pr, Nd, Sm, Eu, Tb, Dy, Ho, Er, Tm, Yb). Dalton Trans. **42**, 10778 (2013)
233. G. Dingemans, A. Clark, J.A. van Delft, M.C.M. van de Sanden, W.M.M. Kessels, Er^{3+} and Si luminescence of atomic layer deposited Er-doped Al_2O_3 thin films on Si(100). J. Appl. Phys. **109**, 113107 (2011)
234. A. Polman, Erbium implanted thin film photonic materials. J. Appl. Phys. **82**, 1 (1997)
235. T. Trupke, M.A. Green, P. Würfel, Improving solar cell efficiencies by down-conversion of high-energy photons. J. Appl. Phys. **92**, 1668 (2002)
236. G. Gao, L. Wondraczek, Near-infrared down-conversion in Mn^{2+}–Yb^{3+} co-doped Zn_2GeO_4. J. Mater. Chem. C **2013**, 1 (1952)

http://www.springer.com/978-3-319-32021-2

Nanomaterials for Sustainable Energy
Li, Q. (Ed.)
2016, XVII, 590 p. 292 illus., 36 illus. in color.,
Hardcover
ISBN: 978-3-319-32021-2